

In silico discovery of representational relationships across visual cortex

Alessandro T. Gifford^{1,2,3,*} , Maya A. Jastrzębowska¹ ,
Johannes J.D. Singer¹ , Radosław M. Cichy^{1,2,3,4} 

¹ Freie Universität Berlin, Berlin, Germany

² Einstein Center for Neurosciences Berlin, Berlin, Germany

³ Bernstein Center for Computational Neuroscience Berlin, Berlin, Germany

⁴ Berlin School of Mind and Brain, Berlin, Germany

* Correspondence: alessandro.gifford@gmail.com

Human vision is mediated by a complex interconnected network of cortical brain areas jointly representing visual information. While these areas are increasingly understood in isolation, their representational relationships remain elusive. Here we developed relational neural control (RNC), and used it to investigate the representational relationships for univariate and multivariate fMRI responses of early- and mid-level visual areas. RNC generated and explored in silico fMRI responses for large amounts of images, discovering controlling images that align or disentangle responses across areas, thus indicating their shared or unique representational content. A large portion of representational content was shared across areas, unique representational content increased with cortical distance, and we isolated the visual features determining these effects. Closing the empirical cycle, we validated the in silico discoveries on in vivo fMRI responses from independent subjects. Together, this reveals how visual areas jointly represent the world as an interconnected network.

Introduction

Human vision is mediated by a complex interconnected network of cortical areas that jointly represent visual information^{1,3,4,7-12}. The network consists of hierarchies and loops, with each area distinctly responding to visual properties of incoming visual stimuli, resulting in idiosyncratic representations of visual phenomena^{2,13-16}.

Over the last half century, taking an atomistic approach, neuroscientists have studied visual representations by characterizing each area in isolation of other areas in a hypothesis-driven fashion using small, limited sets of stimuli carefully chosen by the experimenter. Seminal work in this spirit built the foundations of modern vision neuroscience, from characterizing the role of primary visual cortex for processing of oriented edges⁵ to the role of higher-level visual cortex for processing of complex visual categories such as faces, places and objects⁶.

However, assessing areas one by one does not capture the visual system as an interconnected network; it does not assess representational relationships between areas and thus remains silent about what representational content is shared between areas or unique to a specific area. While anatomical³ and functional¹⁷ connectivity research assess the visual system at the network level, they miss what representational content the network encodes. Compounding the situation, theories of visual representations are based on sparse neural data for small sets of experimenter-picked stimuli, risking to reproduce experimenter biases while missing important neural signals that would be available from broad sampling.

Here, we addressed these challenges by developing relational neural control (RNC), and used it to reveal the representational relationships between early- and mid-level visual areas in humans (i.e., V1, V2, V3, V4). First, through deep-neural-network-based encoding models¹⁸⁻²⁰, RNC generated these areas' in silico fMRI responses for a larger set of naturalistic images than are available in vivo. This in turn enabled the evaluation of a larger, more diverse and thus less biased hypothesis space. Next, to uncover representational relationships, RNC selected controlling images aligning or disentangling the areas' in silico fMRI responses at both their univariate (i.e., voxel average)^{6,21-23} and multivariate (i.e., voxel population pattern)^{21,22,24-26} response level, under the assumption that alignment or disentanglement are indicative of shared or unique representational content, respectively. Finally, we validated our in silico findings in vivo through new experiments on independent subjects, thus closing the empirical cycle and validating RNC as a powerful exploratory neural control method for investigating representational relationships.

Results

RNC provides accurate and denoised in silico fMRI responses for thousands of images

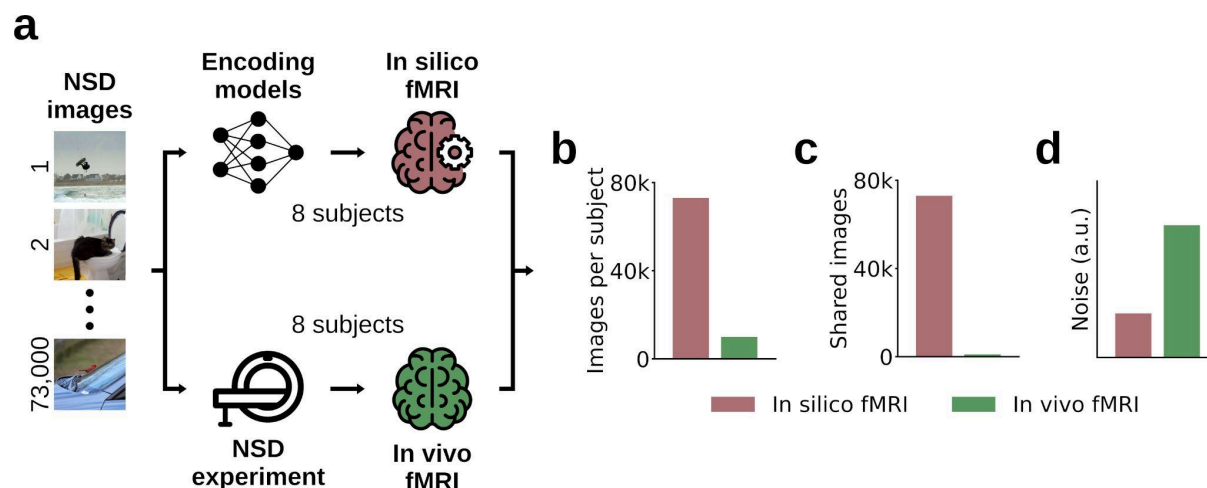


Fig. 1 | In silico vs. in vivo fMRI responses comparison. **a**, Through encoding models, we generated in silico fMRI responses to each of the 73,000 images and for each of the 8 subjects in the natural scenes dataset (NSD). We then compared these in silico responses with the in vivo fMRI responses from the NSD. **b**, Comparison of the number of image conditions presented to each subject, for the in silico and in vivo fMRI responses. **c**, Comparison of the number of image conditions shared across subjects, for the in silico and in vivo fMRI responses. **d**, Comparison of in silico and in vivo fMRI response noise, in arbitrary units.

Using RCN, we determined the representational relationships between human early- and mid-level cortical visual areas (V1, V2, V3, V4).

The first step was creating high-quality in silico brain responses for a large set of visual stimuli (**Fig. 1a**). For this we used the natural scenes dataset (NSD)²⁷, a large-scale dataset of 7T fMRI responses from 8 subjects who each viewed ca. 10,000 natural scenes, for a total of 73,000 images across subjects, with 1,000 images shared across subjects. We trained subject-specific encoding models for areas V1 to V4, mapping image activations from a visual artificial deep neural network onto voxel-wise fMRI responses (**Supplementary Fig. 1a**). The trained encoding models accurately predicted fMRI responses not used for training, resulting in a subject-average explained variance score of 65.94% for V1, 59.71% for V2, 52.92% for V3, and 44.45% for V4 (**Supplementary Fig. 1b**). Using the trained encoding models, we generated in silico fMRI responses to all 73,000 NSD images for each of the 8 subjects, thus increasing the number of image-specific brain responses per subject by a factor of ~7 (**Fig. 1b**).

This had three advantages. First, the large number of responses allowed for wider exploration than possible with in vivo data, thus reducing experimental biases inherent in small data sets. Second, as the in-silico-generated fMRI responses for the whole 73,000 images were present for all subjects, this allowed for more robust cross-subject validation

than would be possible using the in vivo responses to only 1,000 shared images from the NSD (**Fig. 1c**), thus reducing overfitting. Finally, since neural noise is not predictable from the stimulus images, encoding models modeled the signal- and not noise-related variability of the neural response¹⁹, thus resulting in silico fMRI responses less affected by noise compared to the NSD responses (**Fig. 1d**; for the noise comparison see **Supplementary Fig. 1c-d**).

Together, this provided the basis for revealing representational relationships.

RNC controls in silico univariate fMRI responses across cortical areas

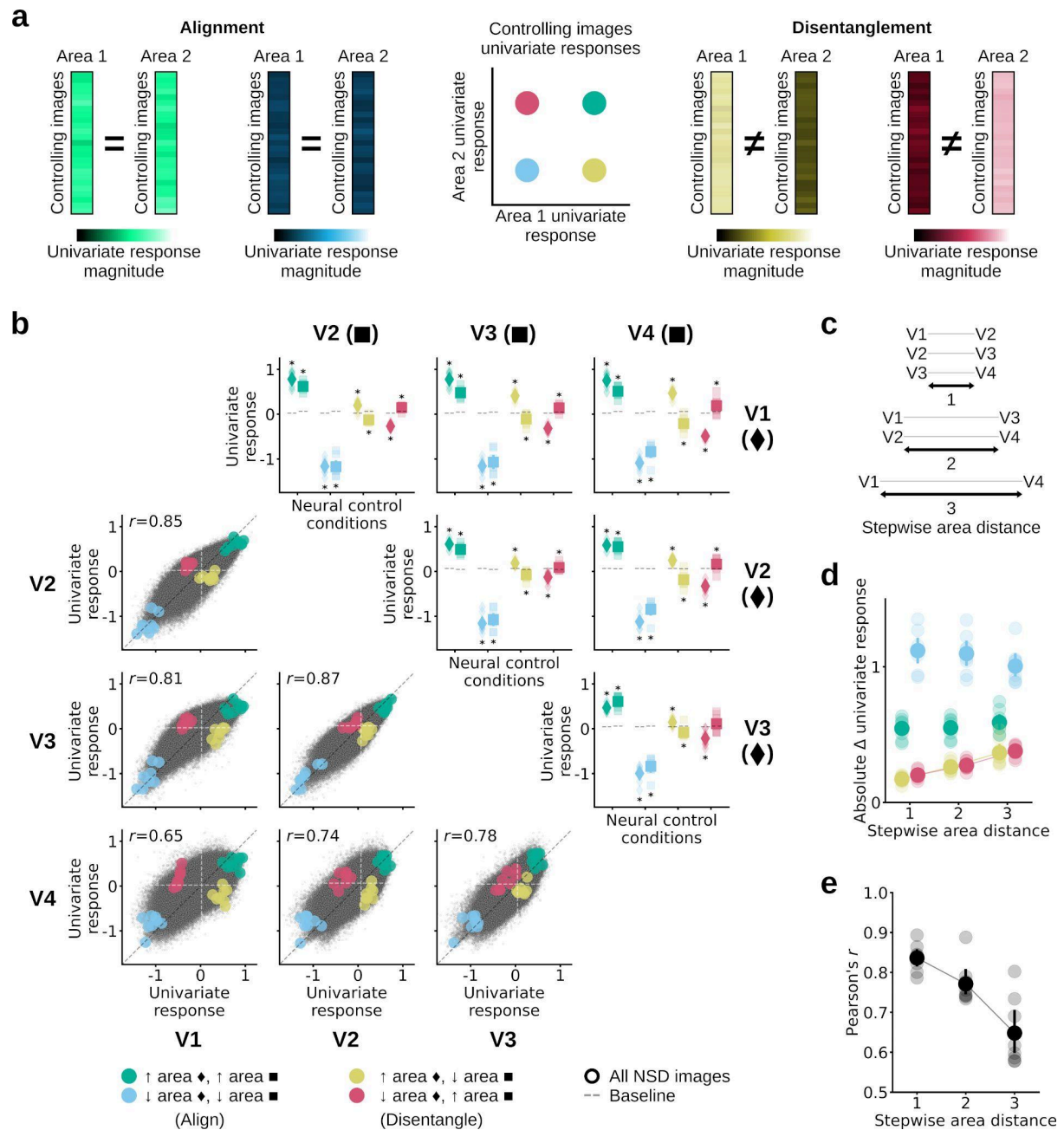


Fig. 2 | Univariate RNC. **a**, Univariate RNC neural control conditions. **b**, Univariate RNC results, embedded in a four-by-four matrix. The upper triangular matrix shows the univariate responses for the controlling images against the baseline. Diamonds and squares indicate the univariate responses of the areas indexed by the rows and columns of the results matrix, respectively. Asterisks indicate neural control conditions for which the in silico univariate fMRI responses for the controlling images are significantly different from baseline ($p < 0.05$, paired-samples one-sided t -test, Benjamini/Hochberg corrected, $n = 8$ subjects). The lower triangular matrix shows the univariate response image manifolds. Colored dots indicate in silico univariate fMRI responses averaged across the controlling images of each neural control condition, and small black points indicate in silico univariate fMRI responses of all subjects for all 73,000 NSD images. Vertical and horizontal dashed lines indicate subject-average univariate response baseline for each

area. **c**, Stepwise distances between areas. **d**, Absolute difference between controlling and baseline images univariate responses, averaged across all pairwise comparisons of areas with same stepwise distance. Connectors between area distances indicate a significant increasing trend ($p < 0.05$, Page test, $n = 8$ subjects). **e**, Correlation between univariate responses in two areas, averaged across pairwise comparisons of areas with same stepwise distance. Connectors between area distances indicate a significant decreasing trend ($p < 0.05$, Page test, $n = 8$ subjects). Opaque and transparent diamonds/squares/dots represent subject-average and single subject results, respectively. Error bars reflect 95% confidence intervals.

We began by investigating representational relationships for in silico univariate fMRI responses (i.e., the average activity over all voxels within an area), thus capturing visual information encoded in the strongest activation trends common across voxels^{6,21–23}.

For each pairwise comparison of areas (V1 vs. V2, V1 vs. V3, V1 vs. V4, V2 vs. V3, V2 vs. V4, V3 vs. V4), we used univariate RNC to search, across all 73,000 NSD images, for images that would either align or disentangle (i.e., control) the in silico univariate fMRI responses of the two areas being compared, thus indicating shared or unique representational content, respectively. Alignment consisted in two neural control conditions where the univariate responses of both areas were either driven or suppressed. Disentanglement consisted in two neural control conditions where the univariate response of one area was driven while the response of the other area suppressed, or vice versa (**Fig. 2a**; the univariate RNC algorithm is visualized in **Supplementary Fig. 3**). To assess the success of the neural control conditions, we compared them against a baseline of univariate responses for a set of images selected without optimization. We used cross-subject validation, thus ensuring generalization of results.

For all neural control conditions, through univariate RNC we found images that significantly drove and suppressed univariate responses of all pairwise comparisons of areas ($p < 0.05$, paired-samples one-sided t -test, Benjamini/Hochberg corrected, $n = 8$ subjects), except for V4's univariate response in the neural control condition suppressing V3 while driving V4 (**Fig. 2b**, upper triangular matrix). Thus, we successfully aligned or disentangled different areas at the univariate response level. For each pairwise comparison of areas, we then visualized the in silico fMRI response manifolds for all 73,000 images in univariate activity space and found their activation profiles to be highly correlated, suggesting that a large portion of representational content is shared across areas (**Fig. 2b**, lower triangular matrix).

Visual areas V1 to V4 form a processing hierarchy in terms of anatomical connectivity⁹, response latency²⁸, and the complexity of stimulus properties maximally driving neural responses¹. This suggests that disentanglement should increase with increasing node distance across this hierarchy. We confirmed this prediction: as the stepwise distance between two areas increased, the absolute difference between the univariate fMRI responses in the disentangling control condition and the baseline increased ($p < 0.05$, Page test, $n = 8$ subjects), indicating that the univariate responses of areas further away from each other were more strongly disentangled (**Fig. 2c-d**). Strengthening this finding, as the stepwise distance between two areas increased, the correlation between their univariate responses decreased ($p < 0.05$, Page test, $n = 8$ subjects) (**Fig. 2e**).

We ascertained that the demonstrated representational relationships reflect general properties of early- and mid-level visual areas, rather than biases of specific image sets, by obtaining qualitatively similar results when applying univariate RNC on the in silico fMRI responses for two out-of-distribution image sets^{29,30} (i.e., single objects presented centrally on natural backgrounds, as opposed to the NSD's complex natural scenes consisting of several or no objects appearing at different locations) (**Supplementary Fig. 4-5**).

Together, through univariate RNC we discovered controlling images that align or disentangle the in silico univariate fMRI responses of multiple areas, revealing that a large portion of univariate responses representational content is shared between areas, and that unique representational content increases as a function of cortical distance.

Spatial frequency and object-like shapes determine unique representational content for V1 and V4 in silico univariate fMRI responses

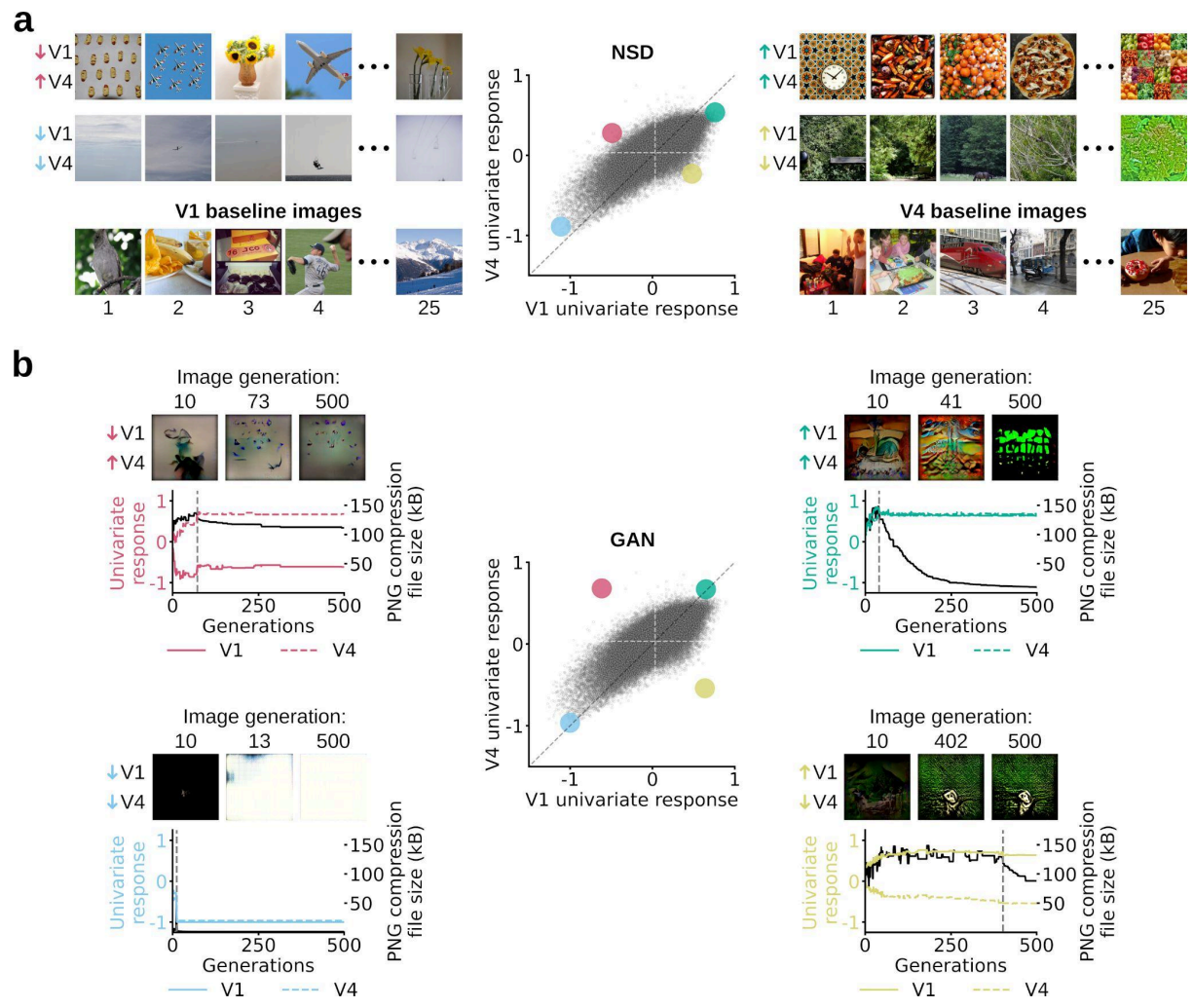


Fig. 3 | Univariate RNC image solutions. **a**, V1 vs. V4 neural control scores and controlling/baseline images obtained by applying univariate RNC jointly on the in silico fMRI responses of all 8 subjects for the 73,000 NSD images. **b**, Generative univariate RNC results. For each neural control condition, the plots show the subject-average in silico univariate fMRI responses (represented by colored lines) and the PNG compression file size (represented by black lines) for the best GAN-generated image of each genetic algorithm optimization generation. The vertical dashed line indicates the generation where the univariate response threshold is reached, after which PNG compression file size starts decreasing. For each plot, the central image comes from the threshold genetic optimization generation.

To determine the visual features leading to aligned or disentangled responses of different areas, we visualized the controlling images that aligned and disentangled their univariate responses. Here we exemplarily focus on the V1 vs. V4 comparison (**Fig. 3a**; the controlling images for all pairwise comparisons of areas are presented in **Supplementary Fig. 6-11**).

The controlling images driving V1 while suppressing V4 responses contained high spatial frequency backgrounds (e.g., vegetation), whereas the controlling images driving V4 while suppressing V1 responses contained one or multiple objects on a low spatial frequency background (e.g., a plane on a sky background). Controlling images driving or suppressing both areas simultaneously were the logical combination thereof: high spatial frequency and objects were present in controlling images driving the response of both areas (e.g., cluttered food items), whereas they were lacking in controlling images suppressing the response of both areas (e.g., empty skies) (**Fig. 3a**). As expected, we discerned no consistent visual patterns in the baseline images (**Fig. 3a**). We made equivalent observations when applying univariate RNC on in silico fMRI responses for out-of-distribution image sets (**Supplementary Fig. 6**), ensuring the robustness of the findings. This showed, through large-scale exploratory analysis using naturalistic images, that V1 is uniquely tuned to high spatial frequency content^{31,32}, whereas V4 is uniquely tuned to object-like shapes³³.

Naturalistic images are complex combinations of multiple visual features making it challenging to isolate, by mere visual inspection, the features leading to aligned or disentangled responses across areas. To further isolate the relevant visual features, we generated de novo controlling images that controlled univariate responses, while being as simple as possible. To this end, we combined RNC with an image generator³⁴ and genetic optimization^{35,36} to iteratively generate images following two serial objectives. The first objective, active throughout the entire optimization procedure, was to generate images controlling (i.e., driving or suppressing) in silico univariate fMRI responses of V1 and V4 up to a threshold. Once this threshold was reached, the second objective became activated, which was to lower image complexity as measured by the images' PNG compression file size^{37,38}. This promoted the generation of one image for each neural control condition containing only the visual features strictly necessary to align or disentangle in silico univariate fMRI responses (**Fig. 3b**; the generative univariate RNC algorithm is visualized in **Supplementary Fig. 12**; for a fine-grained progression of images across generations see **Supplementary Fig. 13**).

Inspection of the genetically optimized images converged with the insights previously gained by naturalistic images. The genetically optimized image driving V1 while suppressing V4 consisted of a uniform high spatial frequency pattern, whereas the image driving V4 while suppressing V1 consisted of multiple small object-like shapes on a uniform background. The images driving or suppressing both areas were again logical combinations of the previous cases: the image driving both areas consisted of many small object-like shapes clustered together, and the image suppressing both areas consisted of a uniform white background.

Together, this shows that high spatial frequencies and object-like shapes are the visual properties leading to unique representational content for V1 and V4 in silico univariate fMRI responses.

RNC controls in silico multivariate fMRI responses across cortical areas

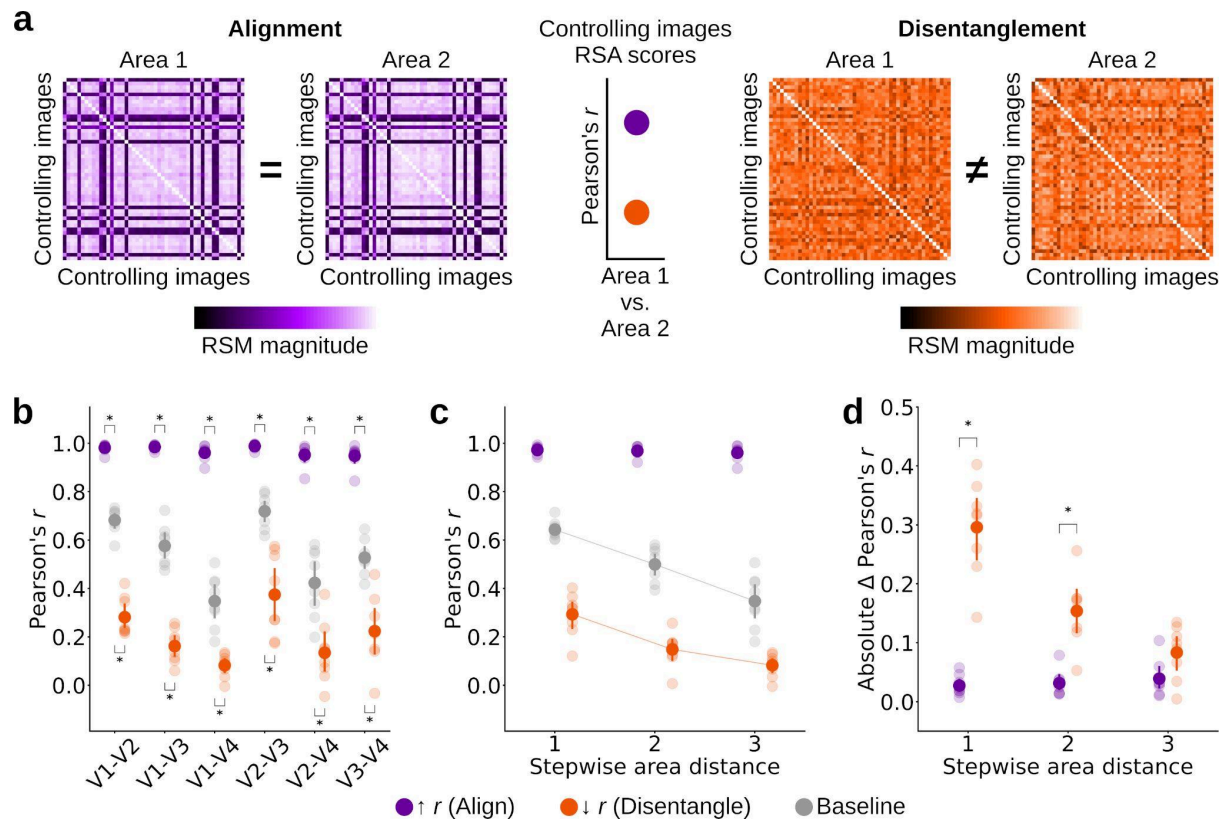


Fig. 4 | Multivariate RNC. **a**, Multivariate RNC neural control conditions. **b**, Multivariate RNC results. Asterisks indicate neural control conditions for which the RSA scores from the controlling images are significantly higher (alignment) or lower (disentanglement) than baseline ($p < 0.05$, paired-samples one-sided t -test, Benjamini/Hochberg corrected, $n = 8$ subjects). **c**, Multivariate RNC RSA scores, averaged across pairwise comparisons of areas with same stepwise distance. Connectors between area distances indicate a significant decreasing trend ($p < 0.05$, Page test, $n = 8$ subjects). **d**, Absolute Pearson's r difference between the observed multivariate RNC RSA scores and the target RSA scores (i.e., $r = 1$ for the alignment neural control condition, and $r = 0$ for the disentanglement neural control condition), averaged across pairwise comparisons of areas with same stepwise distance. Asterisks indicate a significant difference between the difference scores for the aligning and disentangling conditions ($p < 0.05$, paired-samples one-sided t -test, Benjamini/Hochberg corrected, $n = 8$ subjects). Opaque and transparent dots represent subject-average and single subject results, respectively. Error bars reflect 95% confidence intervals.

We next used RNC to reveal the representational relationships for visual information encoded in in silico multivariate fMRI responses (i.e., the population response patterns over all voxels within an area, rather than averaged voxel responses)^{21,22,24–26}.

To control in silico multivariate fMRI responses across areas, their response patterns must be directly comparable to each other. We thus transformed response patterns into representational similarity matrices (RSMs), capturing the representational geometry of each area in a common format²⁵. For each pairwise comparison of areas, we used multivariate

RNC and genetic optimization^{35,36,39,40} to search, across all 73,000 NSD images, for controlling image batches that would either align or disentangle the RSMs of the two areas being compared. Alignment consisted in an image batch leading to a high representational similarity analysis (RSA)²⁵ correlation score (i.e., Pearson's r) for the RSMs of the two areas. Disentanglement consisted in an image batch leading to a low absolute RSA correlation score for the RSMs of the two areas (**Fig. 4a**; the multivariate RNC algorithm is visualized in **Supplementary Fig. 14**). The results were cross-subject validated and compared to a baseline RSM defined on an image batch selected without optimization.

Through multivariate RNC we found controlling image batches that significantly aligned and disentangled the RSMs of all pairwise comparisons of areas ($p < 0.05$, paired-samples one-sided t -test, Benjamini/Hochberg corrected, $n = 8$ subjects) (**Fig. 4b**; for the genetic optimization curves see **Supplementary Fig. 15**). Thus, we successfully aligned or disentangled different areas at the multivariate response level.

Here too we tested whether disentanglement of multivariate responses increases with increasing node distance across the visual processing hierarchy. The RSA scores for the disentangling and baseline images decreased as the stepwise distance between two areas increased ($p < 0.05$, Page test, $n = 8$ subjects), indicating that the multivariate responses of areas further away from each other were more strongly disentangled (**Fig. 4c**). Furthermore, the absolute difference between the observed and target RSA scores were lower for the aligning images for stepwise distance values of one and two, but not three ($p < 0.05$, paired-samples one-sided t -test, Benjamini/Hochberg corrected, $n = 8$ subjects), indicating that areas closer to each other could be more strongly aligned than disentangled (**Fig. 4d**).

We verified the generalizability of these representational relationships, observing qualitatively similar results when applying multivariate RNC on the in silico fMRI responses for out-of-distribution image sets (**Supplementary Fig. 16-17**).

Together, through multivariate RNC we discovered controlling images that align or disentangle the in silico multivariate fMRI responses of multiple areas, revealing that while a large portion of representational content is shared between multivariate responses across visual areas, unique representational content increases as a function of cortical distance.

Shared representational content for V1 and V4 in silico multivariate fMRI responses stems from similar retinotopic properties

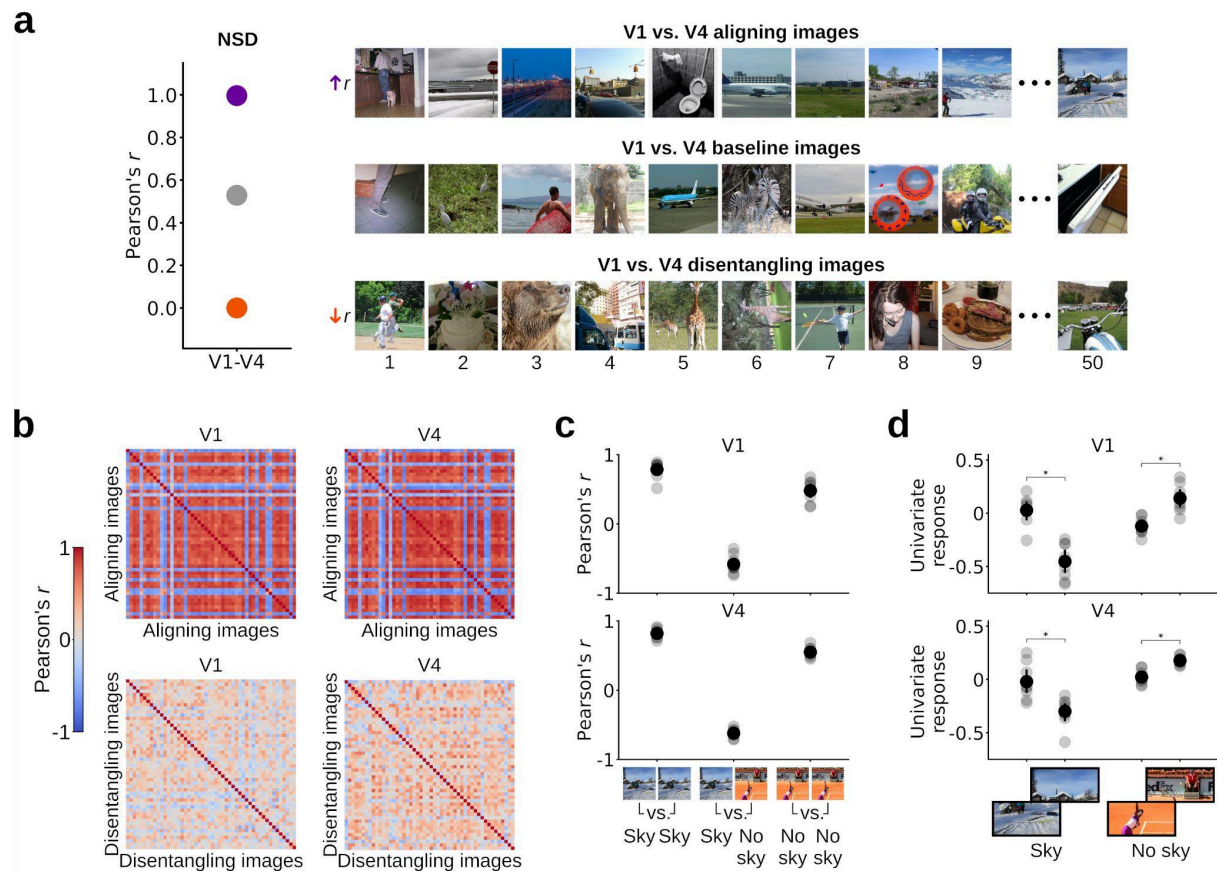


Fig. 5 | Multivariate RNC image solutions. **a**, V1 vs. V4 neural control scores and controlling/baseline images obtained by applying multivariate RNC jointly on the in silico fMRI responses of all 8 subjects for the 73,000 NSD images. **b**, V1 and V4 subject-average RSMs for the multivariate RNC aligning and disentangling images. **c**, V1 and V4 aligning images RSMs mean Pearson's r scores across all comparisons of two sky images, two no sky images, or sky and no sky images. **d**, V1 and V4 mean univariate response for aligning images that either contain or do not contain the sky in their upper half, divided into voxels tuned to the lower and upper part of the visual field. Asterisks indicate a significant difference between the univariate responses of voxels tuned to the lower and upper part of the visual field ($p < 0.05$, paired-samples one-sided t-test, Benjamini/Hochberg corrected, $n = 8$ subjects). Opaque and transparent dots represent subject-average and single subject results, respectively. Error bars reflect 95% confidence intervals.

Which visual features underlie the representational relationships captured in multivariate responses? Here we focus on the V1 vs. V4 comparison (**Fig. 5a**; the controlling images for all pairwise comparisons of areas are presented in **Supplementary Fig. 18-23**).

The aligning images often contained uniform portions (i.e., the sky on their upper half), whereas the disentangling images did not, and the baseline images did but to a lesser extent (**Fig. 5a**). This was also the case when applying multivariate RNC to in silico fMRI responses for out-of-distribution image sets (**Supplementary Fig. 18**).

To understand the effect of image properties on the multivariate RNC scores, we inspected the V1 and V4 RSMs in conjunction with the controlling images (**Fig. 5b**). For both areas, RSM entries comparing different images including the sky in their upper half indicated highly positive correlations, while RSM entries comparing images with and without the sky in the upper half indicated highly negative correlations (**Fig 5c; Supplementary Fig. 24a**). This similar combination of highly positive and negative correlation RSM entries led to a high RSA correlation score for V1 and V4 and thus to alignment. On the other hand, the V1 and V4 RSMs for the disentangling images contained correlation scores of lower absolute magnitude and did not reveal common visual patterns (**Fig. 5b**).

Combining the insights gained from inspecting controlling images and RSMs, we stipulated that retinotopic organization determines neural alignment⁴¹: uniform regions on a spatially constrained portion of the image will lead to suppressed responses for V1 and V4 voxels tuned to the corresponding portion of the visual field, in turn leading to aligned RSMs for the two areas.

We tested this hypothesis by comparing the V1 and V4 univariate responses of voxels tuned to the upper and lower portion of the visual field, for aligning images including uniform regions (i.e., the sky) in their upper half. As predicted, for both areas we found that the univariate response of voxels was lower for the upper than for the lower visual field ($p < 0.05$, paired-samples one-sided t -test, Benjamini/Hochberg corrected, $n = 8$ subjects) (**Fig. 5d**), explaining why RSM entries comparing different images including the sky in their upper half resulted in highly positive correlations (**Supplementary Fig. 24b**). We observed the opposite pattern when comparing voxel responses for aligning images not including the sky in their upper half ($p < 0.05$, paired-samples one-sided t -test, Benjamini/Hochberg corrected, $n = 8$ subjects) (**Fig. 5d**), explaining why RSM entries comparing images with and without the sky in the upper half resulted in highly negative correlations (**Supplementary Fig. 24b**).

Together, these results point to common retinotopic properties as a source of shared representational content in V1 and V4 in silico multivariate fMRI responses.

In-silico-discovered controlling images control in vivo fMRI responses of independent subjects

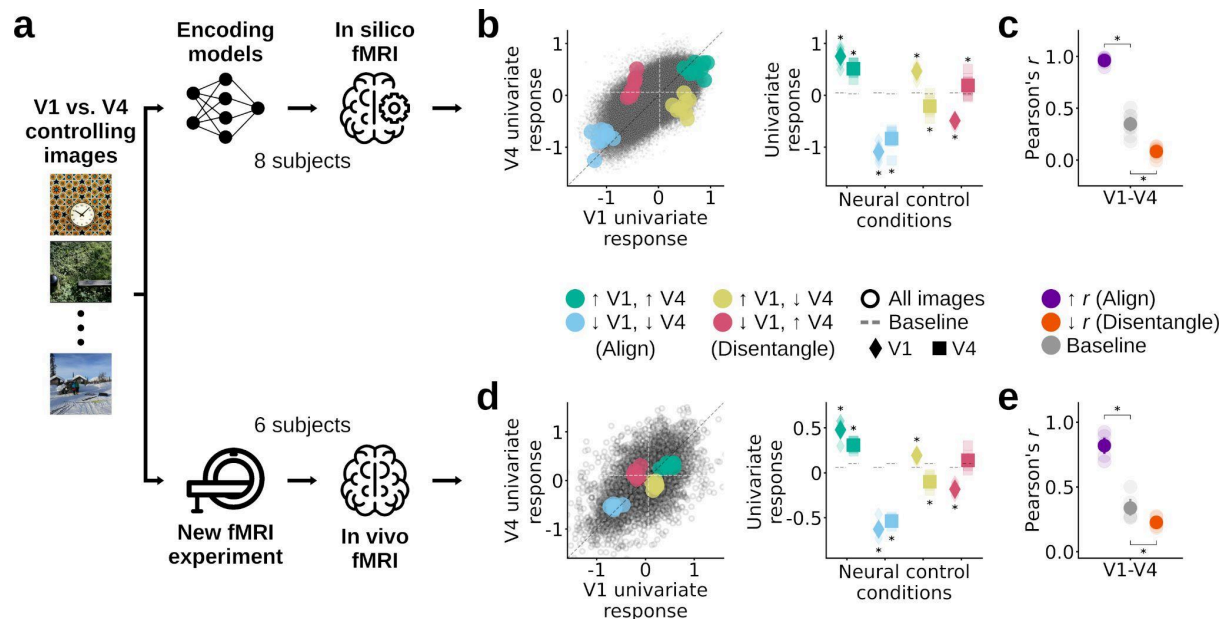


Fig. 6 | In vivo validation of RNC solutions. **a**, We tested whether the images controlling univariate and multivariate in silico fMRI responses for the V1 vs. V4 comparison generalized their control effect to in vivo fMRI responses of six new, independent subjects. **b**, Univariate RNC in silico results. **c**, Multivariate RNC in silico results. **d**, Univariate RNC in vivo results. **e**, Multivariate RNC in vivo results. Asterisks indicate a significant effect of the controlling images with respect to baseline ($p < 0.05$, paired-samples one-sided t -test, Benjamini/Hochberg corrected, $n = 8$ subjects for the in silico analyses, $n = 6$ subjects for the in vivo analyses). Opaque and transparent dots/diamonds/squares represent subject-average and single subject results, respectively. Error bars reflect 95% confidence intervals.

In silico discoveries empower and accelerate empirical research, but do not replace it: these discoveries need to be validated empirically. Thus, we complemented the above results for areas V1 and V4 – which were cross-subject validated on in silico fMRI responses – with empirical validation on in vivo fMRI responses.

We conducted an fMRI experiment where we presented an independent set of subjects ($n = 6$) with the univariate and multivariate RNC controlling images for the V1 vs. V4 comparison (**Fig. 6a**; for the experimental design see **Supplementary Fig. 25a**). We defined V1 and V4 in the new subjects using population receptive field (pRF) mapping⁴² (an illustration of the pRF experiment and the V1/V4 delineations are presented in **Supplementary Fig. 25b-c**). We found that the controlling images aligned and disentangled both univariate (**Fig. 6d**) and multivariate (**Fig. 6e**) responses of V1 and V4 in these new subjects, ($p < 0.05$, paired-samples one-sided t -test, Benjamini/Hochberg corrected, $n = 6$ subjects), except for V4's univariate response in the univariate neural control condition suppressing V1 while driving V4.

The successful generalization to in vivo fMRI responses closed the empirical cycle, confirming the in silico discoveries and validating RNC as a new exploratory neural control method for investigating representational relationships.

Discussion

We investigated representational relationships between early- and mid-level visual areas of the human cortex using relational neural control (RNC). Through RNC, we extensively explored in silico fMRI responses for a vast collection of naturalistic images, finding controlling images that aligned or disentangled univariate and multivariate in silico fMRI responses across areas, thus indicating shared or unique representational content. Closing the empirical cycle, we validated the in silico discoveries on in vivo fMRI responses by presenting the controlling images to independent subjects.

Representations are the key concept in theories of information processing in visual cortex^{2,4,14,15,43,44}, and because visual processing is supported by the concerted effort of multiple areas^{1,3,7-12}, understanding how visual cortex works requires a joint investigation of the representational relationships between such areas. Thus, RNC invites a perspective shift from asking “What does each area represent?”, to asking “What is the *relationship* between representations in different areas?” RNC answers the latter question by applying neural control^{35,36,45-51} jointly to multiple cortical areas, thus determining the causal role of specific visual input to their aligned or disentangled visual representations^{45,52}. Hence, RNC extends existing anatomical³ and functional¹⁷ connectivity research assessing the brain as a complex interconnected network with the concept of representation. Representations being the material of information processing and transfer^{2,4,53}, our results promote the understanding of how perception and cognition emerge from the joint interaction of the representational content of multiple cortical areas.

RNC successfully controlled univariate and multivariate in silico fMRI responses jointly for areas V1, V2, V3 and V4, resulting in a quantitative and qualitative characterization of the representational relationships between these areas¹. Quantitatively, we found that unique representational content for a given pair of areas increased as a function of their cortical distance along the visual hierarchy, both in the case of univariate and multivariate responses. This representational pattern likely reflects the decrease in anatomical connectivity with increasing distance between visual areas⁹, as well as other gradual changes along the visual hierarchy such as increasing receptive field sizes⁵⁴ and increasingly complex functional specialization¹. Qualitatively, we isolated the visual features indicating shared or unique representational content for V1 and V4. The features aligning and disentangling univariate responses (i.e., spatial frequency³¹ and object-like shapes³³) were different from the ones aligning and disentangling multivariate responses (i.e., topological image properties⁴¹). Thus, the univariate and multivariate response levels captured complementary aspects of representational relationships between areas, suggesting that visual cortex multiplexes diverse neural codes for visual information processing^{4,53,55} and, in turn, encouraging the integrated analysis of diverse neural response levels.

RNC embodies a research paradigm combining the advantages of in silico neural response exploration with empirical validation of findings on in vivo neural responses^{56,57}. In silico exploration takes the power of recently emerging large-scale in vivo neural datasets^{27,58-60} to the next level. In vivo neural responses are available in limited numbers and are expensive and slow to acquire. In contrast, after initial training on an in vivo dataset, encoding models cheaply and quickly generate in silico neural responses to any amount and type of stimuli,

thus allowing for unprecedentedly large upscaling of the solution spaces on which to explore and test scientific hypotheses. Moreover, encoding models generate *in silico* neural responses which are less affected by noise compared to *in vivo* responses, thus reducing the effect of noise on results¹⁹. Together, this allows exploration of a much larger amount of stimuli and corresponding neural responses, effectively reducing the risk of sub-optimal or biased findings deriving from smaller and noisier samples or from experimenter's hand-picked stimuli.

The key limitation of RNC lies in the component that empowers it: the encoding models generating the *in silico* neural responses do not predict all explainable neural signal, and their predictions generalize imperfectly beyond the distribution of the visual data they were trained on. However, the current push in the development of better visual encoding models^{61–63} based on large *in vivo* data sets^{27,58–60} promises ever more accurate *in silico* neural responses, in turn increasing the reliability of findings from experimentation on computer-generated brain data.

We note that the assumption of aligned or disentangled neural responses indicating shared or unique representational content is not a given. We found that the assumption was correct for all multivariate RNC control conditions, for the univariate RNC disentanglement conditions, but not for the univariate RNC alignment conditions. There, the controlling images aligning both V1 and V4 univariate fMRI responses consisted of the logical combination of the visual features disentangling them (i.e., high spatial frequency and objects), rather than of features for which the two areas are not disentangled, as would be the case if the assumption held. Together, this highlights a way to rigorously test the assumptions of RNC. Furthermore, finding the assumption to be negated is in itself scientifically interesting, as it reveals how either shared or unique representational content can lead to aligned univariate responses.

A key feature of the RNC paradigm is flexibility. First, it naturally extends to representational relationship research across different types of data: from controlling single voxels to arbitrarily many areas; to investigating different representational relationship properties such as their temporal development or behavioral relevance by control of time series or behavioral data; to the investigation of other sensory modalities, for instance through control of auditory or language neural responses⁶⁴; as well as to exploring unique and shared representational content within artificial information processing systems. Second, RNC can uncover complementary aspects of representational relationships by controlling other neural response levels than univariate or multivariate activations such as variance across fMRI voxels, neural oscillations⁶⁵, neural latent spaces⁶⁶, or geometric manifolds properties⁶⁷. Finally, RNC can support comparative research by jointly controlling responses of distinct information processing systems to uncover shared or unique representational content between individuals⁶⁸, species⁶⁹, or between biological and artificial intelligence systems⁷⁰.

To promote RNC adoption we created [Colab tutorials](#) where users can interactively implement univariate and multivariate RNC on the Neural Encoding Dataset (NED) (<https://github.com/gifale95/NED>): *in silico* fMRI responses for ~150,000 naturalistic images spanning the entire visual cortex.

In sum, using RNC we uncovered the representational relationships between human early- and mid-level visual areas. This demonstrates the power of *in silico* exploration combined with *in vivo* validation to reveal how human cortical areas, at the level of networks, collectively represent the visual world.

Methods

Encoding models

The trained fMRI encoding models used to generate the in silico fMRI responses are available as part of the Neural Encoding Dataset (NED) (<https://github.com/gifale95/NED>). Below we describe how we trained and tested these models.

Data

We trained encoding models of fMRI responses to images on the Natural Scenes Dataset (NSD)²⁷, a large-scale dataset of 7T fMRI responses from 8 subjects who each viewed up to 10,000 distinct color images of natural scenes. Out of these 10,000 images, 9,000 were subject-unique (i.e., only seen by individual subjects), and 1,000 were shared (i.e., seen by all subjects). Each image was presented up to three times, for a maximum of 30,000 trials per subject.

We used the NSD preprocessed fMRI responses in subject-native volume space ("func1pt8mm") from betas version 3 ("betas_fithrf_GLMdenoise_RR") and selected voxels falling within areas V1, V2, V3 and V4 (using the "prf-visualroi" area definitions provided by the NSD). For each NSD scanning session, we z-scored the responses of each voxel across all trials of that session.

For each subject, we split the data into training, validation and testing partitions. The training partition consisted of the fMRI responses for the 9,000 subject-unique images. The testing partition consisted of the 515/1,000 shared images that were presented to all subjects three times (to maximize the reliability of the data on which the models were tested). The validation partition consisted of the remaining 485/1,000 shared images that were not presented to all subjects three times.

Model architecture

As encoding models, we used the feature-weighted receptive field (fwRF), a convolutional neural network trained end-to-end to predict fMRI responses to images^{27,71}. Each fwRF encoding model predicted fMRI responses for multiple voxels – in our case, we trained one fwRF model for all voxels of each subject and area.

The fwRF consists of one backbone (shared across all voxels) and of multiple projection heads (one for each voxel). The shared backbone is a multi-layer feedforward convolutional neural network called GNet²⁷. Giving an image as input to GNet activates its layers, resulting in multiple features maps (i.e., GNet's representations of this image). The weights of this backbone are fully learned during model training, jointly for all voxels.

The projection heads consist of a spatial pooling field and of feature weights. The spatial pooling field determines the region of visual space (i.e., the GNet feature space which, due to the convolutional operations, preserves the topology of visual space of the input images) that drives voxel activity. After the backbone's feature maps are spatially pooled, they are linearly

combined by the feature weights, resulting in the voxel response prediction. Both the spatial pooling field and feature weights are learned during model training, independently for each voxel.

Model training

We trained a separate encoding model for each NSD subject and area (V1, V2, V3, V4), resulting in 8 subjects \times 4 areas = 32 encoding models. To reduce spurious statistical dependencies between the in silico (i.e., model-generated) fMRI responses from models of different subjects and areas, we trained each model starting from a different random initialization⁷².

Given an input image, the fwRF model's objective was to minimize the mean squared error between the predicted fMRI responses (for all voxels of a given subject and area) and the corresponding target fMRI responses. During training, the mean squared error loss was backpropagated and the model weights updated (**Supplementary Fig. 1a**). At each backpropagation step, the projection head weights were only optimized based on the loss of their corresponding voxel, whereas the backbone weights were optimized based on the loss combined over all voxels. We trained the models using single (i.e., not averaged) NSD trials.

We optimized the fwRF encoding model weights on the training data partition, using batch sizes of 128 images and the Adam optimizer with a learning rate of 0.001, a weight decay term of 0, and the default value for the remaining hyperparameters. We trained the models on 75 data epochs and retained the model weights from the epoch leading to lowest loss between predicted and target fMRI responses, using the validation data partition.

Model testing

We used the trained models to generate in silico fMRI responses for the test data partition images and compared them with the corresponding target responses, averaged across the three trials, using Pearson's correlation. We computed the correlation independently for each voxel across the 515 test images, and squared the resulting correlation coefficients to obtain r^2 , the total variance explained by the models. We then divided the r^2 score of each voxel with that voxel's noise ceiling, resulting in a measure of explained variance quantifying the portion of the explainable variance (given the noise in the data) that had been accounted for by the models. We tested the models independently for each voxel and subject, and then averaged the results across voxels belonging to the same subject and area (**Supplementary Fig. 1b**).

Noise analysis

Because neural noise is not predictable from the stimulus images, encoding models model the signal- and not noise-related variability of the neural response¹⁹, thus resulting in silico fMRI responses less affected by noise compared to in vivo responses. To establish this empirically, we compared the noise of the in silico fMRI responses with the noise of the in vivo fMRI responses from the NSD, by comparing how much variance these two data types explained for a third, independent split of the in vivo NSD responses. Because the in silico neural responses did not capture all signal variance in the NSD responses (**Supplementary Fig. 1b**), the in silico neural responses explaining more variance than the in vivo NSD responses would be indicative of the former being less affected by noise. We carried out the

comparison through three sets of predictions, using the in silico and the in vivo NSD fMRI responses for the 515 test images (**Supplementary Fig. 1c**), and the same explained variance metric described in the previous paragraph “Model testing”. Each prediction involved explaining in vivo single NSD experiment response trials with a different predictor. In the first set of predictions, the predictor consisted of one of the two remaining in vivo NSD experiment response trials. We conducted six such predictions, such that each of the three in vivo NSD trials was used as the target to be explained and each of the two remaining in vivo NSD trials was used as a predictor. We then averaged the explained variance scores from the six different predictions. In the second set of predictions, the predictor consisted of the average of the two remaining in vivo NSD experiment response trials. We conducted three such predictions, each time using one of the three in vivo NSD trials as the target to be explained and the average of the remaining two in vivo NSD trials as the predictor. We then averaged the explained variance scores from the three different predictions. In the third set of predictions, the predictor consisted of the in silico responses from the trained encoding models. We repeated the prediction three times, each time using one of the three in vivo NSD trials as the target to be explained and the corresponding in silico responses as the predictor. We averaged the explained variance scores from the three different predictions. We carried out these comparisons independently for each voxel and subject, and averaged the results across voxels belonging to the same subject and area.

Noise ceiling derivation

We derived the noise ceiling of each voxel from its noise ceiling signal-to-noise ratio (ncsnr) score, provided by the NSD and computed on z-scored fMRI betas. For each voxel, the ncsnr quantified the ratio of the signal standard deviation over the noise standard deviation:

$$ncsnr = \frac{\hat{\sigma}_{signal}}{\hat{\sigma}_{noise}}$$

The noise standard deviation was obtained by calculating the variance of the betas across the three presentations of each image (using the unbiased estimator that normalizes by $n-1$ where n is the sample size), averaging this variance across images, and then computing the square root of the result:

$$\hat{\sigma}_{noise} = \sqrt{\text{mean}(\beta_{\sigma}^2)}$$

where β_{σ}^2 indicates the variance across the betas obtained for a given image. Given that the variance of the z-scored betas is 1, the signal standard deviation was estimated as:

$$\hat{\sigma}_{signal} = \sqrt{\left|1 - \hat{\sigma}_{noise}^2\right|_+}$$

where $||_+$ indicates positive half-wave rectification. Finally, we used the ncsnr scores to derive the noise ceiling (NC) of each voxel as:

$$NC = 100 \times \frac{ncsnr^2}{ncsnr^2 + \frac{1}{n}}$$

where n indicates the number of trials that are averaged together. We used $n = 3$ when evaluating the encoding models against the NSD test responses averaged across all three trials (**Supplementary Fig. 1b**), and $n = 1$ during the noise analysis, since there we considered single trials as the target to be explained (**Supplementary Fig. 1c**).

In silico fMRI responses generation

Image sets

We used the trained encoding models of each subject and area to generate in silico fMRI responses for the 73,000 images from the NSD, depicting complex natural scenes consisting of several or no objects appearing at different locations. We additionally generated fMRI responses for two out-of-distribution (with respect to NSD images) image sets depicting single objects presented centrally on natural backgrounds: 50,000 images from the ImageNet 2012 challenge validation split³⁰; and 26,107 images from THINGS²⁹.

Voxel selection

To prevent results being biased towards noisy voxels, for all subsequent analyses we only used in silico fMRI responses for voxels with a noise ceiling signal-to-noise ratio (ncsnr) above 0.5 (for the amount of retained voxels, see **Supplementary Table 1**).

Univariate RNC

The goal of univariate relational neural control (RNC) was to search the 73,000 NSD images for images that controlled (i.e., aligned or disentangled) the in silico univariate fMRI responses – that is, averaged responses across all voxels of a given given area – of each pairwise comparison of areas (V1 vs. V2, V1 vs. V3, V1 vs. V4, V2 vs. V3, V2 vs. V4, V3 vs. V4). We additionally applied univariate RNC to the images and corresponding fMRI responses for the out-of-distribution image sets (i.e., ImageNet and THINGS).

Univariate RNC baseline

For each area, we randomly selected a batch of 25 images (out of all 73,000 NSD images), fed them into the given area's encoding model, and averaged the corresponding in silico univariate fMRI responses across the 25 images, resulting in a single score corresponding to the mean fMRI response for that image batch. By repeating this step 1 million times, we created the univariate RNC null distribution and selected the 25 images from the batch with scores closest to the null distribution mean. The mean univariate response score across these 25 images provided the area-wise univariate response baseline against which we tested the neural control scores from the controlling images selected through univariate RNC.

Univariate RNC algorithm

We fed the 73,000 NSD images to the trained encoding models of two areas, and averaged the resulting in silico fMRI responses across voxels, obtaining a one-dimensional univariate response vector of length 73,000 for each of the two areas. We then either summed (alignment) or subtracted (disentanglement) the univariate response vectors of the two areas and ranked the resulting sum/difference scores. Finally, we kept the 25 controlling images that yielded the highest or lowest (depending on the neural control condition) scores and, at the same time, resulted in in silico univariate fMRI responses higher or lower than the areas' univariate response baselines by a margin of at least 0.04.

This resulted in four sets of 25 controlling images, each set corresponding to a different neural control condition. The controlling images from the sum vector led to two neural control conditions in which the two areas have aligned univariate responses (i.e., images that either drive or suppress the responses of both areas), whereas the controlling images from the difference vector led to two neural control conditions in which the two areas have disentangled univariate responses (i.e., images that drive the responses of one area while suppressing the responses of the other area, or vice versa) (the univariate RNC algorithm is visualized in **Supplementary Fig. 3**).

Subject-wise cross-validation

We used subject-wise leave-one-out cross-validation to evaluate the univariate RNC solutions (as well as the baseline) by selecting the controlling images based on the *in silico* univariate fMRI responses averaged across seven subjects and evaluating them on the *in silico* univariate fMRI responses of the left out subject. We repeated cross-validation for each unique set of seven subjects, resulting in eight cross-validated solutions.

Generative univariate RNC

Generative univariate RNC used an image generator and genetic optimization to generate stimulus images leading to aligned or disentangled *in silico* univariate fMRI responses for V1 and V4, while at the same time being as simple as possible.

We began by creating 1,000 random latent vectors from a standard normal distribution (each vector being 4,096-dimensional). We gave the latent vectors as input to DeePSiM³⁴, a pre-trained generative adversarial network (GAN), which used them to generate 1,000 images, and clamped the output image pixel values to the valid RGB range [0 255]. We stored the PNG compression file sizes of these images, as well as their latent vectors, for later use during the genetic optimization.

We then fed the generated images to the V1 and V4 trained encoding models of all subjects, and averaged the resulting *in silico* fMRI responses across both voxels and subjects, obtaining a one-dimensional univariate response vector of length 1,000, for both V1 and V4. We stored the univariate responses of both areas for later use during the genetic optimization. Depending on the univariate RNC neural control condition being optimized, we then either summed or subtracted the univariate response vectors of the two areas and stored these sum or difference scores.

Next, we fed the latent vectors, the PNG compression file sizes, the V1 and V4 univariate responses, and the sum/difference scores to a genetic optimization algorithm^{35,36}, which used these inputs to create a new generation of latent vectors. Optimization consisted of two phases. At first, the objective of the genetic optimization was to create new latent vectors leading to images more likely to result in univariate responses closer to threshold level. Once the univariate response threshold was reached, the objective switched to creating new latent vectors leading to images more likely to have lower PNG compression file sizes, while at the same time keeping the univariate responses above threshold.

This resulted in a new batch of 1,000 latent vectors, which we fed to the GAN for the second optimization generation, repeating the same steps. After 500 genetic optimization generations, we obtained a single image (i.e., the best performing image from the last genetic optimization generation) that optimally controlled univariate neural responses following one of four univariate RNC neural control conditions, while at the same time being as simple as possible (i.e., having a low PNG compression file size). We optimized the images for the four neural control conditions independently of each other (the generative univariate RNC algorithm is visualized in **Supplementary Fig. 12**).

For each area, the univariate response threshold consisted in the area's univariate response baseline plus a margin of 0.6 (for control conditions driving the area's response) or -0.6 (for control conditions suppressing the area's response).

Genetic optimization algorithm

The genetic optimization assigned a global score to each latent vector. If a latent vector led to univariate responses below threshold level for at least one of the two areas, its global score consisted in the corresponding sum/difference score, plus a large penalty (10^{10}). If a latent vector led to univariate responses above threshold level for both V1 and V4, its global score consisted in the PNG compression file size of the corresponding image. Since the penalty value was constant, the global scores of several latent vectors leading to below-threshold univariate responses were ranked based on the corresponding sum/difference scores of these vectors. Thus, until the threshold was reached, the latent vectors were optimized to result in better sum/difference scores. Because the sum/difference scores were based on the univariate responses, this in turn led to univariate responses progressively closer to threshold level. Furthermore, since the penalty was always larger than the PNG file sizes, the global scores of latent vectors leading to above-threshold univariate responses always ranked better than the global scores of latent vectors leading to below-threshold univariate responses. This ensured that the optimization would favor latent vectors leading to univariate responses above threshold.

We transformed the global scores of all latent vectors into probabilities through z-scoring, scaling by a factor of 0.5, and passing the resulting values through a softmax function. The genetic optimization algorithm used these probabilities to create a new generation of latent vectors, while balancing exploitation and exploration. Exploitation involved keeping (untouched) the 250 latent vectors with highest probability scores (i.e., the latent vectors leading to either univariate responses closest to threshold or lowest PNG compression file sizes). Exploration involved creating 750 new children latent vectors from recombinations between two parent latent vectors from the current generation, where the likelihood of each latent vector being a parent was determined by its probability score. The two parents contributed unevenly to any one child: 75%/25% of the child latent vector came from the parent latent vector with highest/lowest probability scores, respectively. Finally, during recombination, each of the 4,096 components of a child latent vector had a 0.25 probability of being mutated, with mutations drawn from a 0-centered Gaussian with standard deviation 0.75.

Multivariate RNC

The goal of multivariate relational neural control (RNC) was to search the 73,000 NSD images for images that controlled (i.e., aligned or disentangled) the in silico multivariate fMRI responses – that is, the population response pattern of all voxels of a given area – of each pairwise comparison of areas (V1 vs. V2, V1 vs. V3, V1 vs. V4, V2 vs. V3, V2 vs. V4, V3 vs. V4). We additionally applied multivariate RNC to the images and corresponding fMRI responses for the out-of-distribution image sets (i.e., ImageNet and THINGS).

Multivariate RNC baseline

For each pairwise comparison of areas, we randomly selected a batch of 50 images (out of all 73,000 NSD images), used the encoding models to generate the corresponding in silico fMRI responses, transformed these in silico responses into RSMs, and used representational similarity analysis (RSA)²⁵ to compare the RSMs of the two areas (using Pearson's correlation), resulting in one score for the image batch. By repeating this step 1 million times, we created the multivariate RNC null distribution, and selected the 50 images from the batch with scores closest to the null distribution mean. The RSA score of these 50 images provided the baseline against which we tested the neural control scores from multivariate RNC.

Multivariate RNC algorithm

The multivariate RNC was based on a genetic optimization^{35,36,39,40} which, through 2,000 generations, selected images that best aligned or disentangled the in silico multivariate fMRI responses.

We started by creating 2,400 random batches of 50 images from the 73,000 NSD images, with no repeating image within each batch. We fed these image batches to the trained encoding models of two given areas, and transformed the resulting in silico fMRI responses into representational similarity matrices (RSMs)²⁵, resulting in one 50 × 50 image RSM for each of the 2,400 image batches, and each of the two areas. We then compared the RSMs of each image batch between the two areas using Pearson's correlation, obtained one correlation score (r) for each image batch, and ranked these correlation scores. To align the two areas, we kept the 200 image batches with highest correlation scores (i.e., images most similarly represented by the two areas), whereas to disentangle them, we kept the 200 image batches with lowest absolute correlation scores (i.e., images most differently represented by the two areas). Finally, we used these 200 highest/lowest ranked image batches as input to a genetic optimization algorithm, which used them to create 2,400 image batches, while balancing exploitation and exploration. Exploitation involved creating five mutated versions for each of the 200 image batches. In each version, a different number of images (1, 5, 12, 25, and 38) was randomly replaced with other images out of the 73,000 NSD images, while ensuring that no image repeated within the same batch. This increased the image batches to 1,200 (200 best batches + 200 best batches × 5 mutated versions = 1,200 batches). Exploration involved creating another 1,200 new random batches which, together with the 1,200 batches from the exploitation step, amounted to 2,400 batches of 50 images. During the second optimization generation, we once again fed these 2,400 image batches to the encoding models and repeated the same steps.

We ran 2,000 genetic optimization generations and selected the best performing image batch from the last generation. This resulted in one of two sets of 50 controlling images, each set corresponding to a different neural control condition (the image batches from the two neural control conditions were optimized independently of each other). The controlling images from the ranked correlation vector led to an alignment of multivariate responses in the two areas (i.e., images leading to high Pearson's r scores for the two areas), whereas the controlling images from the absolute ranked correlation vector led to a disentanglement of multivariate responses in the two areas (i.e., images leading to low absolute Pearson's r scores for the two areas) (the multivariate RNC algorithm is visualized in **Supplementary Fig. 14**).

Subject-wise cross-validation

We used subject-wise leave-one-out cross-validation to evaluate the multivariate RNC solutions (as well as the baseline) by selecting the controlling images based on the *in silico* fMRI RSMs averaged across seven subjects, and evaluating them on the *in silico* fMRI RSM of the left out subject. We repeated cross-validation for each unique set of seven subjects, resulting in eight cross-validated solutions.

Definition of lower and upper visual field voxels

For area V1, we selected voxels tuned to the lower and upper portions of the visual field based on the V1d (i.e., V1 dorsal) and V1v (i.e., V1 ventral) NSD delineations, respectively. For area V4, we used the polar angle maps from the NSD population receptive field (pRF) experiment to manually divide the area into voxels tuned to the lower and upper portions of the visual field.

fMRI experiments

Participants

Six healthy adults (mean age 25.83 years, SD = 4.67; 4 female, 2 male) participated; all had normal or corrected-to-normal vision. All subjects provided written informed consent and received monetary reimbursement. Procedures were approved by the ethical committee of the Department of Education and Psychology at Freie Universität Berlin and were in accordance with the Declaration of Helsinki.

Stimuli

During the fMRI experiments, we presented subjects with 150 images from the V1 vs. V4 univariate RNC solutions (25 images from each of the two aligning conditions, 25 images from each of the two disentangling conditions, 25 images from V1's baseline, and 25 images from V4's baseline) (**Fig. 3a**), and 150 images from the V1 vs. V4 multivariate RNC solutions (50 images from aligning condition, 50 images from disentangling condition, and 50 images from the baseline) (**Fig. 5a**). All images were sized 425 pixels × 425 pixels × 3 RGB channels.

To prevent confounds driven by luminance, we matched each image's mean luminance (i.e., its luminance across all pixels) to the luminance of the stimuli presentation screen background (a uniform gray screen with an RGB value of [127 127 127]), using the "ImageEnhance" function from the Pillow Python package (<https://python-pillow.org/>).

Experimental paradigm

Main experiment

Each subject underwent two fMRI data collection sessions. Each session consisted of multiple four-second trials, where an image was presented for two seconds, followed by two seconds of gray screen inter-stimulus interval (**Supplementary Fig. 25a**). To ensure that subjects paid attention, we presented the RNC controlling images within an orthogonal target detection task where we asked subjects to report, through a button press, whenever a catch image containing the fictional character Buzz Lightyear appeared on the screen.

During the first session, we presented the 150 controlling images from univariate RNC, across 10 runs. Each run consisted of 109 four-second trials: it started with 3 blank trials (i.e., a gray screen where no image was presented), continued with a pseudo-randomized order of 90 univariate RNC image trials, 8 blank trials, and 4 catch trials (i.e., images containing Buzz Lightyear), and ended with 4 blank trials. Across all 10 runs, this resulted in 6 presentation repeats for each of the 150 univariate RNC controlling images.

During the second session, we presented the 150 controlling images from multivariate RNC, across 12 runs. Each run consisted of 121 four-second trials: it started with 3 blank trials, continued with a pseudo-randomized order of 100 multivariate RNC image trials, 9 blank trials, and 5 catch trials (i.e., images containing Buzz Lightyear), and ended with 4 blank trials. Across all 12 runs, this resulted in 8 presentation repeats for each of the 150 multivariate RNC controlling images.

All images were presented centrally, with a horizontal and vertical visual angle of 8.4° , against a gray background with an RGB value of [127, 127, 127]. A small semi-transparent red fixation dot with a black border ($0.2^\circ \times 0.2^\circ$, 50% opacity) was present at the center of the images throughout the entirety of both sessions, and we asked subjects to maintain central fixation throughout the experiment. We controlled stimulus presentation using the Psychtoolbox⁷³, and recorded fMRI responses during both experimental sessions.

pRF experiment

We ran the 'multibar' pRF experiment used in the NSD²⁷, which is an adaptation of the pRF experiment used in the Human Connectome Project 7T Retinotopy Dataset⁴². Stimuli consisted of slowly moving apertures filled with a dynamic colorful texture, and involved bars sweeping in multiple directions (same as RETBAR in the Human Connectome Project 7T Retinotopy Dataset) (**Supplementary Fig. 25b**). Apertures and textures were updated at a rate of 16 Hz. Stimuli filled a circular region with diameter 12° . Each run lasted 300 seconds, and included blank periods. Throughout stimulus presentation, a small semi-transparent dot (with diameter 0.2°) was present at the center of the stimuli. The color of the central dot switched randomly to one of three colors (black, white or red) every 1 to 5 seconds. Subjects were instructed to maintain fixation on the dot and to press a button whenever the dot

changed color. To further aid fixation, a semi-transparent fixation grid was superimposed on the stimuli and was present throughout the experiment⁷⁴. For each subject, we collected three runs of the pRF experiment, at the beginning of the first fMRI session.

fMRI

Acquisition

We collected MRI data using a Siemens Magnetom Prisma Fit 3T system (Siemens Medical Solutions, Erlangen, Germany) with a 64-channel head coil.

Anatomical scans were acquired during each recording session using a standard T1-weighted sequence (TR = 1.9 s, TE = 3.22 ms, number of slices 176, FOV = 225 mm, voxel size 1.0 mm isotropic, flip angle 8°).

Functional images were acquired using gradient-echo EPI at 2.5 mm isotropic resolution with partial brain coverage (TR = 1 s, TE = 33 ms, number of axial slices 39, matrix size 82 × 82, FOV = 205 mm, flip angle 70°, acquisition order interleaved, inter-slice gap 0.25 mm, multi-band slice acceleration factor 3). The acquisition volume fully covered the occipital lobe.

Dual-echo fieldmaps were acquired during each recording session (TR = 0.4 s, TE₁ = 4.92 ms, TE₂ = 7.38 ms, number of slices 38, voxel size 3 mm isotropic, matrix size = 66 × 66, FOV = 198 mm, flip angle 60°).

Preprocessing

We preprocessed the fMRI data using SPM12 (<https://www.fil.ion.ucl.ac.uk/spm/software/spm12/>). Preprocessing steps included realigning all functional images to the first image of each run, slice-time correction, field map correction, and co-registration of the functional images to the anatomical image of the first recording session.

pRF mapping

The population receptive field (pRF) mapping analysis was run using the prf-workflow package (<https://github.com/mayajas/prf-workflow>), with the model fitting done with the pRFpy package (v0.1.0; <https://github.com/VU-Cog-Sci/prfpy>). The preprocessed functional data of the three pRF runs were projected to the Freesurfer reconstruction of the white matter cortical surface of the given subject. The surface-projected signals at each surface mesh vertex were detrended to account for linear drifts, bandpass filtered (0.01 to 0.1 Hz) and z-scored over time. The signals from the three pRF runs were then averaged together. We fit an isotropic 2D Gaussian pRF model to the data at each cortical surface vertex, with an initial coarse grid fit followed by a fine iterative fit, to optimize the parameters that define pRF size and the location (x, y) in Cartesian coordinates in visual space that the underlying population of neurons responds to.

The optimized location parameters were transformed to eccentricities and polar angle maps, which we then used to manually delineate visual regions of interest (ROIs) V1 and V4.

Delineations were constrained to the maximum stimulus eccentricity of the controlling images (i.e., 8.4° of visual angle) based on the eccentricity map, while the visual areas were identified based on reversals in the polar angle map. To ensure specificity the visual area delineations were drawn conservatively, with the dorsal/ventral boundaries drawn just ventrally/dorsally of the corresponding polar angle reversal (**Supplementary Fig 25c**).

GLM

We used GLMsingle⁷⁵ to estimate single-trial beta responses (i.e., BOLD response amplitudes evoked by each image trial) of the preprocessed fMRI data from the main experiment. GLMsingle provides single-trial beta estimates following three steps. First, for each voxel, a custom hemodynamic response function (HRF) is identified from a library of candidate functions. Second, cross-validation is used to derive a set of noise regressors from voxels that have negligible amounts of BOLD variance related to the experiment (using an R^2 threshold). Third, to improve the stability of beta estimates for closely spaced trials, betas are regularized on a voxel-wise basis using ridge regression. The resulting betas indicate the percent of BOLD signal change evoked by single image trials, with respect to a baseline corresponding to the absence of a stimulus (i.e., a gray screen with no image presented). We applied GLMsingle with default parameters, independently to the preprocessed fMRI responses of each subject, session, and area (i.e., independently for the voxels of V1 and V4).

Z-scoring and voxel selection

For consistency with the in silico fMRI data, here too we z-scored the beta responses (from GLMsingle) of each voxel across all trials of each session and computed the noise ceiling signal-to-noise ratio (ncsnr) of each voxel. For further analyses, we retained only those voxels with ncsnr scores above 0.4. The more liberal ncsnr threshold (compared to the in silico fMRI data analyses) comes from the fact that not all recorded subjects and areas consisted in voxels with ncsnr scores above 0.5. We computed the ncsnr independently for the data of the two recording sessions, that is, independently for the fMRI responses for the univariate and multivariate RNC images. This resulted in a different amount of retained voxels between the two experimental sessions, which can be seen in **Supplementary Tables 2-3**.

Statistical testing

We used a paired-sample one-sided t -test to assess statistically significant differences between the explained variance scores of the different predictors in the noise analysis, the null hypothesis being that the explained variance scores of the different predictors were equal ($p < 0.05$). We used paired-samples one-sided t -tests to assess statistically significant differences between the univariate and multivariate RNC scores and the corresponding baseline scores, again the null hypothesis being that the different scores were equal ($p < 0.05$). We used paired-samples one-sided t -tests to assess statistically significant differences of the absolute difference of observed and target RSA scores between alignment and disentanglement multivariate RNC scores at each stepwise area distance, the null hypothesis being that the alignment and disentanglement RNC score absolute differences were equal ($p < 0.05$). We used a Page test to assess statistically significant increasing or decreasing trends across stepwise area distances, with a null hypothesis of no increasing or

decreasing trend between scores at different stepwise area distances ($p < 0.05$). We used paired-samples one-sided t -tests to assess statistically significant differences between the univariate responses of voxels tuned to the lower and upper portions of the visual field, the null hypothesis being that the univariate responses in the upper and lower visual fields were equal ($p < 0.05$). The sample sizes of these tests were either $N = 8$ subjects for tests of the in silico fMRI responses, or $N = 6$ for tests on the in vivo fMRI responses from the fMRI experiments.

We controlled familywise error rate by applying (non-negative) Benjamini/Hochberg correction⁷⁶ to the resulting p -values to correct for the number of comparisons ($N = 4$ comparisons, one for each area, for the encoding models noise analysis; $N = 8$ comparisons within each univariate RCN pairwise comparison of areas; $N = 2$ comparisons within each multivariate RCN pairwise comparison of areas; $N = 3$ comparisons when analyzing the multivariate RNC alignment and disentanglement absolute differences at each stepwise area distance; $N = 2$ comparisons when analyzing the upper and lower visual field voxels of each area).

To calculate the confidence intervals of each statistic, we created 100,000 bootstrapped samples by sampling the subject-specific results with replacement. This yielded empirical distributions of the results, from which we derived the 95% confidence intervals.

References

1. Grill-Spector, K. & Malach, R. The Human visual Cortex. *Annu. Rev. Neurosci.* **27**, 649–677 (2004).
2. Kriegeskorte, N. & Diedrichsen, J. Peeling the Onion of Brain Representations. *Annu. Rev. Neurosci.* **42**, 407–432 (2019).
3. Van Essen, D. C., Anderson, C. H. & Felleman, D. J. Information Processing in the Primate Visual System: An Integrated Systems Perspective. *Science* **255**, 419–423 (1992).
4. deCharms, R. C. & Zador, A. Neural Representation and the Cortical Code. *Annu. Rev. Neurosci.* **23**, 613–647 (2000).
5. Hubel, D. H. & Wiesel, T. N. Receptive fields and functional architecture of monkey striate cortex. *J. Physiol.* **195**, 215–243 (1968).
6. Kanwisher, N. Functional specificity in the human brain: A window into the functional architecture of the mind. *Proc. Natl. Acad. Sci.* **107**, 11163–11170 (2010).
7. Barlow, H. B. Why have multiple cortical areas? *Vision Res.* **26**, 81–90 (1986).
8. Bullier, J. Integrated model of visual processing. *Brain Res. Rev.* **36**, 96–107 (2001).
9. Felleman, D. J. & Van Essen, D. C. Distributed hierarchical processing in the primate cerebral cortex. *Cereb. Cortex N. Y. N* **1991** **1**, 1–47 (1991).
10. Kravitz, D. J., Saleem, K. S., Baker, C. I. & Mishkin, M. A new neural framework for visuospatial processing. *Nat. Rev. Neurosci.* **12**, 217–230 (2011).
11. Maunsell, J. H. R. & Newsome, W. T. Visual Processing in Monkey Extrastriate Cortex. *Annu. Rev. Neurosci.* **10**, 363–401 (1987).
12. Milner, A. D. & Goodale, M. A. Two visual systems re-viewed. *Neuropsychologia* **46**, 774–785 (2008).
13. Ballard, D. H. On the Function of Visual Representation. in *Vision and Mind* (eds. Noë, A. & Thompson, E.) 459–480 (The MIT Press, 2002). doi:10.7551/mitpress/7111.003.0020.
14. Barack, D. L. & Krakauer, J. W. Two views on the cognitive brain. *Nat. Rev. Neurosci.* **22**, 359–371 (2021).
15. DiCarlo, J. J., Zoccolan, D. & Rust, N. C. How Does the Brain Solve Visual Object Recognition? *Neuron* **73**, 415–434 (2012).
16. Martin, K. A. C. A Brief History of the “Feature Detector”. *Cereb. Cortex* **4**, 1–7 (1994).
17. Van Den Heuvel, M. P. & Hulshoff Pol, H. E. Exploring the brain network: A review on resting-state fMRI functional connectivity. *Eur. Neuropsychopharmacol.* **20**, 519–534 (2010).
18. Naselaris, T., Kay, K. N., Nishimoto, S. & Gallant, J. L. Encoding and decoding in fMRI. *NeuroImage* **56**, 400–410 (2011).
19. Wu, M. C.-K., David, S. V. & Gallant, J. L. Complete Functional Characterization Of Sensory Neurons By System Identification. *Annu. Rev. Neurosci.* **29**, 477–505 (2006).
20. Yamins, D. L. K. & DiCarlo, J. J. Using goal-driven deep learning models to understand sensory cortex. *Nat. Neurosci.* **19**, 356–365 (2016).
21. Davis, T. *et al.* What do differences between multi-voxel and univariate analysis mean? How subject-, voxel-, and trial-level variance impact fMRI analysis. *NeuroImage* **97**, 271–283 (2014).
22. Hebart, M. N. & Baker, C. I. Deconstructing multivariate decoding for the study of brain function. *NeuroImage* **180**, 4–18 (2018).

23. Kanwisher, N., McDermott, J. & Chun, M. M. The Fusiform Face Area: A Module in Human Extrastriate Cortex Specialized for Face Perception. *J. Neurosci.* **17**, 4302–4311 (1997).
24. Haynes, J.-D. & Rees, G. Decoding mental states from brain activity in humans. *Nat. Rev. Neurosci.* **7**, 523–534 (2006).
25. Kriegeskorte, N., Mur, M. & Bandettini, P. A. Representational similarity analysis - connecting the branches of systems neuroscience. *Front. Syst. Neurosci.* **2**, (2008).
26. Mur, M., Bandettini, P. A. & Kriegeskorte, N. Revealing representational content with pattern-information fMRI—an introductory guide. *Soc. Cogn. Affect. Neurosci.* **4**, 101–109 (2009).
27. Allen, E. J. *et al.* A massive 7T fMRI dataset to bridge cognitive neuroscience and artificial intelligence. *Nat. Neurosci.* **25**, 116–126 (2022).
28. Schmolesky, M. T. *et al.* Signal Timing Across the Macaque Visual System. *J. Neurophysiol.* **79**, 3272–3278 (1998).
29. Hebart, M. N. *et al.* THINGS: A database of 1,854 object concepts and more than 26,000 naturalistic object images. *PLOS ONE* **14**, e0223792 (2019).
30. Russakovsky, O. *et al.* ImageNet Large Scale Visual Recognition Challenge. *Int. J. Comput. Vis.* **115**, 211–252 (2015).
31. Foster, K. H., Gaska, J. P., Nagler, M. & Pollen, D. A. Spatial and temporal frequency selectivity of neurones in visual cortical areas V1 and V2 of the macaque monkey. *J. Physiol.* **365**, 331–363 (1985).
32. Kay, K. N., Naselaris, T., Prenger, R. J. & Gallant, J. L. Identifying natural images from human brain activity. *Nature* **452**, 352–355 (2008).
33. Kobatake, E. & Tanaka, K. Neuronal selectivities to complex object features in the ventral visual pathway of the macaque cerebral cortex. *J. Neurophysiol.* **71**, 856–867 (1994).
34. Dosovitskiy, A. & Brox, T. Generating Images with Perceptual Similarity Metrics based on Deep Networks. in *Advances in Neural Information Processing Systems* vol. 29 (Curran Associates, Inc., 2016).
35. Ponce, C. R. *et al.* Evolving Images for Visual Neurons Using a Deep Generative Network Reveals Coding Principles and Neuronal Preferences. *Cell* **177**, 999–1009.e10 (2019).
36. Xiao, W. & Kreiman, G. XDream: Finding preferred stimuli for visual neurons using generative networks and gradient-free optimization. *PLOS Comput. Biol.* **16**, e1007973 (2020).
37. Marin, M. M. & Leder, H. Examining Complexity across Domains: Relating Subjective and Objective Measures of Affective Environmental Scenes, Paintings and Music. *PLoS ONE* **8**, e72412 (2013).
38. Mayer, S. & Landwehr, J. R. Quantifying visual aesthetics based on processing fluency theory: Four algorithmic measures for antecedents of aesthetic preferences. *Psychol. Aesthet. Creat. Arts* **12**, 399–431 (2018).
39. Vaziri, S., Carlson, E. T., Wang, Z. & Connor, C. E. A Channel for 3D Environmental Shape in Anterior Inferotemporal Cortex. *Neuron* **84**, 55–62 (2014).
40. Yamane, Y., Carlson, E. T., Bowman, K. C., Wang, Z. & Connor, C. E. A neural code for three-dimensional object shape in macaque inferotemporal cortex. *Nat. Neurosci.* **11**, 1352–1360 (2008).
41. Wandell, B. A. & Winawer, J. Imaging retinotopic maps in the human brain. *Vision Res.* **51**, 718–737 (2011).

42. Benson, N. C. *et al.* The Human Connectome Project 7 Tesla retinotopy dataset: Description and population receptive field analysis. *J. Vis.* **18**, 23 (2018).
43. DiCarlo, J. J. & Cox, D. D. Untangling invariant object recognition. *Trends Cogn. Sci.* **11**, 333–341 (2007).
44. Marr, D. Visual information processing: the structure and creation of visual representations. *Philos. Trans. R. Soc. Lond. B Biol. Sci.* **290**, 199–218 (1980).
45. Bashivan, P., Kar, K. & DiCarlo, J. J. Neural population control via deep image synthesis. *Science* **364**, eaav9436 (2019).
46. Gu, Z. *et al.* NeuroGen: Activation optimized image synthesis for discovery neuroscience. *NeuroImage* **247**, 118812 (2022).
47. Lehky, S. R., Sejnowski, T. J. & Desimone, R. Predicting responses of nonlinear neurons in monkey striate cortex to complex patterns. *J. Neurosci.* **12**, 3568–3581 (1992).
48. Ratan Murty, N. A., Bashivan, P., Abate, A., DiCarlo, J. J. & Kanwisher, N. Computational models of category-selective brain regions enable high-throughput tests of selectivity. *Nat. Commun.* **12**, 5540 (2021).
49. Walker, E. Y. *et al.* Inception loops discover what excites neurons most using deep predictive models. *Nat. Neurosci.* **22**, 2060–2065 (2019).
50. Wang, B. & Ponce, C. R. Tuning landscapes of the ventral stream. *Cell Rep.* **41**, 111595 (2022).
51. Wang, T. *et al.* Large-scale calcium imaging reveals a systematic V4 map for encoding natural scenes. *Nat. Commun.* **15**, 6401 (2024).
52. Jazayeri, M. & Afraz, A. Navigating the Neural Space in Search of the Neural Code. *Neuron* **93**, 1003–1014 (2017).
53. Perkel, D. H. & Bullock, T. H. Neural coding. *Neurosci. Res. Program Bull.* **6**, 221–348 (1968).
54. Dumoulin, S. O. & Wandell, B. A. Population receptive field estimates in human visual cortex. *NeuroImage* **39**, 647–660 (2008).
55. Xie, W. *et al.* Neuronal sequences in population bursts encode information in human cortex. *Nature* (2024) doi:10.1038/s41586-024-08075-8.
56. Jain, S., Vo, V. A., Wehbe, L. & Huth, A. G. Computational Language Modeling and the Promise of In Silico Experimentation. *Neurobiol. Lang.* **5**, 80–106 (2024).
57. Mathis, M. W., Perez Rotondo, A., Chang, E. F., Tolia, A. S. & Mathis, A. Decoding the brain: From neural representations to mechanistic models. *Cell* **187**, 5814–5832 (2024).
58. Gifford, A. T., Dwivedi, K., Roig, G. & Cichy, R. M. A large and rich EEG dataset for modeling human visual object recognition. *NeuroImage* **264**, 119754 (2022).
59. Hebart, M. N. *et al.* THINGS-data, a multimodal collection of large-scale datasets for investigating object representations in human brain and behavior. *eLife* **12**, e82580 (2023).
60. Lahner, B. *et al.* BOLD Moments: modeling short visual events through a video fMRI dataset and metadata. Preprint at <https://doi.org/10.1101/2023.03.12.530887> (2023).
61. Gifford, A. T. *et al.* The Algonauts Project 2023 Challenge: How the Human Brain Makes Sense of Natural Scenes. Preprint at <https://doi.org/10.48550/ARXIV.2301.03198> (2023).
62. Schrimpf, M. *et al.* Brain-Score: Which Artificial Neural Network for Object Recognition is most Brain-Like? Preprint at <https://doi.org/10.1101/407007> (2018).
63. Willeke, K. F. *et al.* The Sensorium competition on predicting large-scale mouse primary visual cortex activity. Preprint at <https://doi.org/10.48550/ARXIV.2206.08666> (2022).
64. Tuckute, G. *et al.* Driving and suppressing the human language network using large language models. *Nat. Hum. Behav.* 1–18 (2024) doi:10.1038/s41562-023-01783-7.

65. Buzsáki, G. & Draguhn, A. Neuronal Oscillations in Cortical Networks. *Science* **304**, 1926–1929 (2004).
66. Cunningham, J. P. & Yu, B. M. Dimensionality reduction for large-scale neural recordings. *Nat. Neurosci.* **17**, 1500–1509 (2014).
67. Chung, S. & Abbott, L. F. Neural population geometry: An approach for understanding biological and artificial neural networks. *Curr. Opin. Neurobiol.* **70**, 137–144 (2021).
68. Charest, I., Kievit, R. A., Schmitz, T. W., Deca, D. & Kriegeskorte, N. Unique semantic space in the brain of each beholder predicts perceived similarity. *Proc. Natl. Acad. Sci.* **111**, 14565–14570 (2014).
69. Orban, G. A., Van Essen, D. & Vanduffel, W. Comparative mapping of higher visual areas in monkeys and humans. *Trends Cogn. Sci.* **8**, 315–324 (2004).
70. Doerig, A. *et al.* The neuroconnectionist research programme. *Nat. Rev. Neurosci.* **24**, 431–450 (2023).
71. St-Yves, G. & Naselaris, T. The feature-weighted receptive field: an interpretable encoding model for complex feature spaces. *NeuroImage* **180**, 188–202 (2018).
72. Mehrer, J., Spoerer, C. J., Kriegeskorte, N. & Kietzmann, T. C. Individual differences among deep neural network models. *Nat. Commun.* **11**, 5725 (2020).
73. Brainard, D. H. The Psychophysics Toolbox. *Spat. Vis.* **10**, 433–436 (1997).
74. Schira, M. M., Tyler, C. W., Breakspear, M. & Spehar, B. The Foveal Confluence in Human Visual Cortex. *J. Neurosci.* **29**, 9050–9058 (2009).
75. Prince, J. S. *et al.* Improving the accuracy of single-trial fMRI response estimates using GLMsingle. *eLife* **11**, e77599 (2022).
76. Benjamini, Y. & Hochberg, Y. Controlling the False Discovery Rate: A Practical and Powerful Approach to Multiple Testing. *J. R. Stat. Soc. Ser. B Stat. Methodol.* **57**, 289–300 (1995).

Acknowledgments

A.T.G. is supported by a PhD fellowship of the Einstein Center for Neurosciences. M.A.J. is supported by the Horizon Europe Framework Programme (HORIZON-MSCA-2021-PF-01, grant number: 101064539). R.M.C. is supported by German Research Council (DFG) grants (CI 241/1-1, CI 241/1-3, CI 241/1-7, INST 272/297-1) and the European Research Council (ERC) starting grant (ERC-StG-2018-803370). We thank the HPC Service of FUB-IT, Freie Universität Berlin, for computing time. We thank Kendrick Kay for helpful feedback, and Ian Charest for help with the Natural Scenes Dataset.

Author contributions

A.T.G. and R.M.C. designed research. A.T.G., J.J.D.S. and M.A.J. acquired fMRI data. A.T.G. and J.J.D.S. preprocessed fMRI data. A.T.G. and M.A.J. performed population receptive field analyses. A.T.G. modeled and analyzed data. A.T.G. and R.M.C. interpreted results. A.T.G. prepared figures. A.T.G. drafted the manuscript. A.T.G., J.J.D.S., M.J. and R.M.C. edited and revised the manuscript. All authors approved the final version of the manuscript.

Competing interests

The authors declare no competing interests.

Data availability

The univariate and multivariate RNC algorithms were applied on in silico fMRI responses from the Neural Encoding Dataset (<https://github.com/gifale95/NED>).





The controlling images for all pairwise comparisons of areas, along with the in vivo fMRI responses for the V1 vs. V4 comparison controlling images, are available on OpenNeuro (<https://openneuro.org/datasets/ds005503>).

Code availability

The code to reproduce all the paper results, along with the RNC interactive tutorials, are available on GitHub (<https://github.com/gifale95/RNC>).

Supplementary information

In silico discovery of representational relationships across visual cortex

Alessandro T. Gifford^{1,2,3,*} , Maya A. Jastrzębowska¹ ,
Johannes J.D. Singer¹ , Radoslaw M. Cichy^{1,2,3,4} 

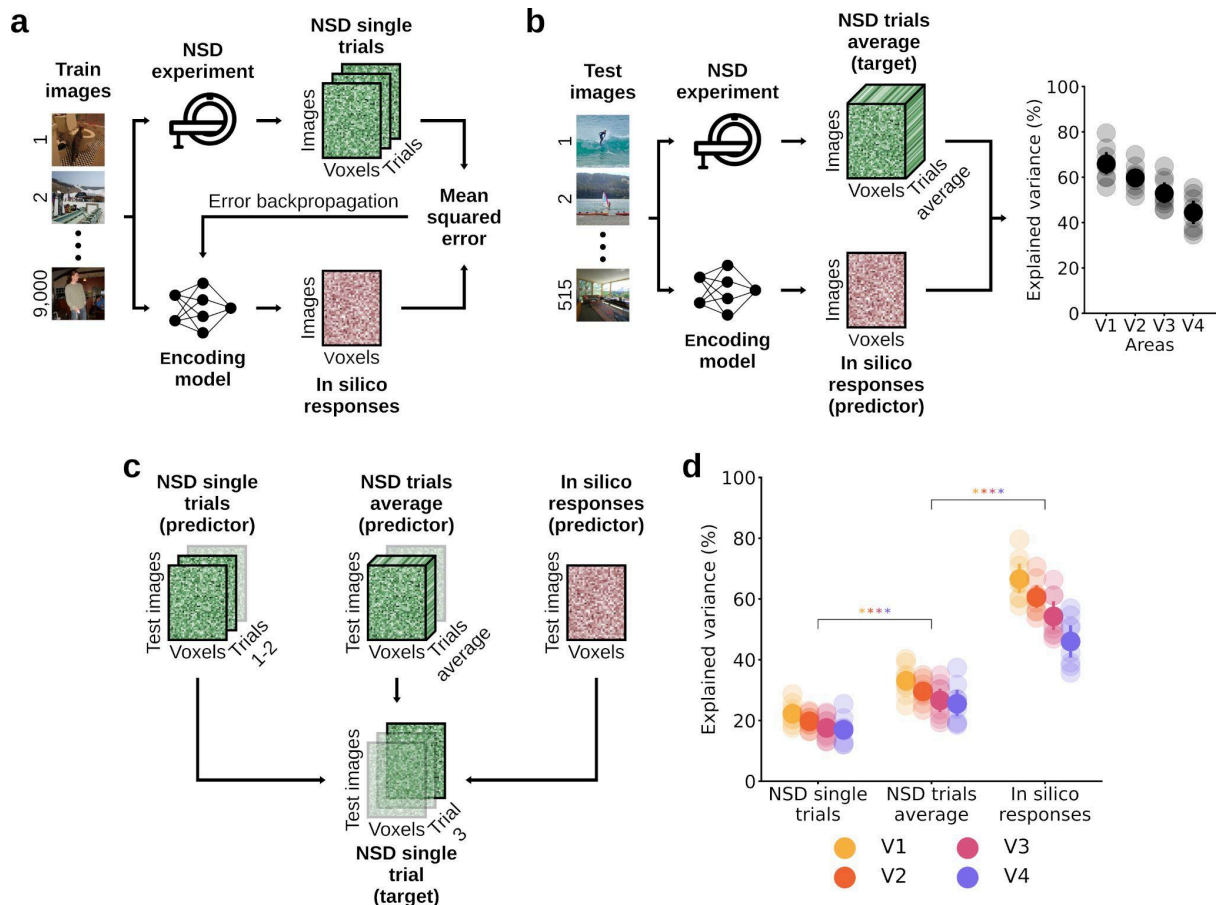
¹ Freie Universität Berlin, Berlin, Germany

² Einstein Center for Neurosciences Berlin, Berlin, Germany

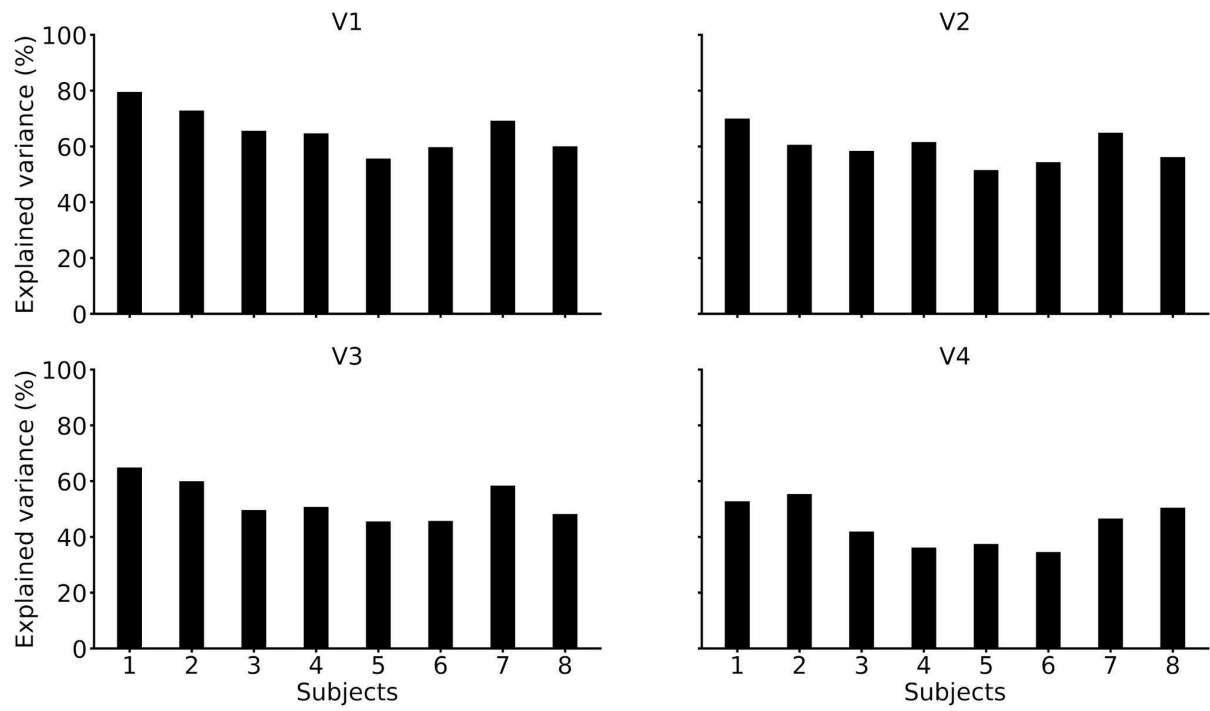
³ Bernstein Center for Computational Neuroscience Berlin, Berlin, Germany

⁴ Berlin School of Mind and Brain, Berlin, Germany

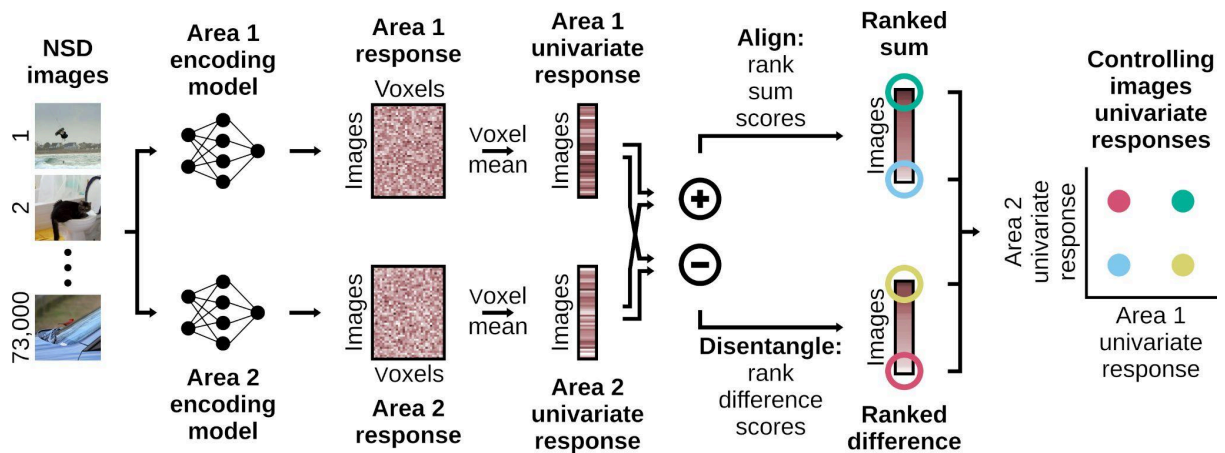
* Correspondence: alessandro.gifford@gmail.com



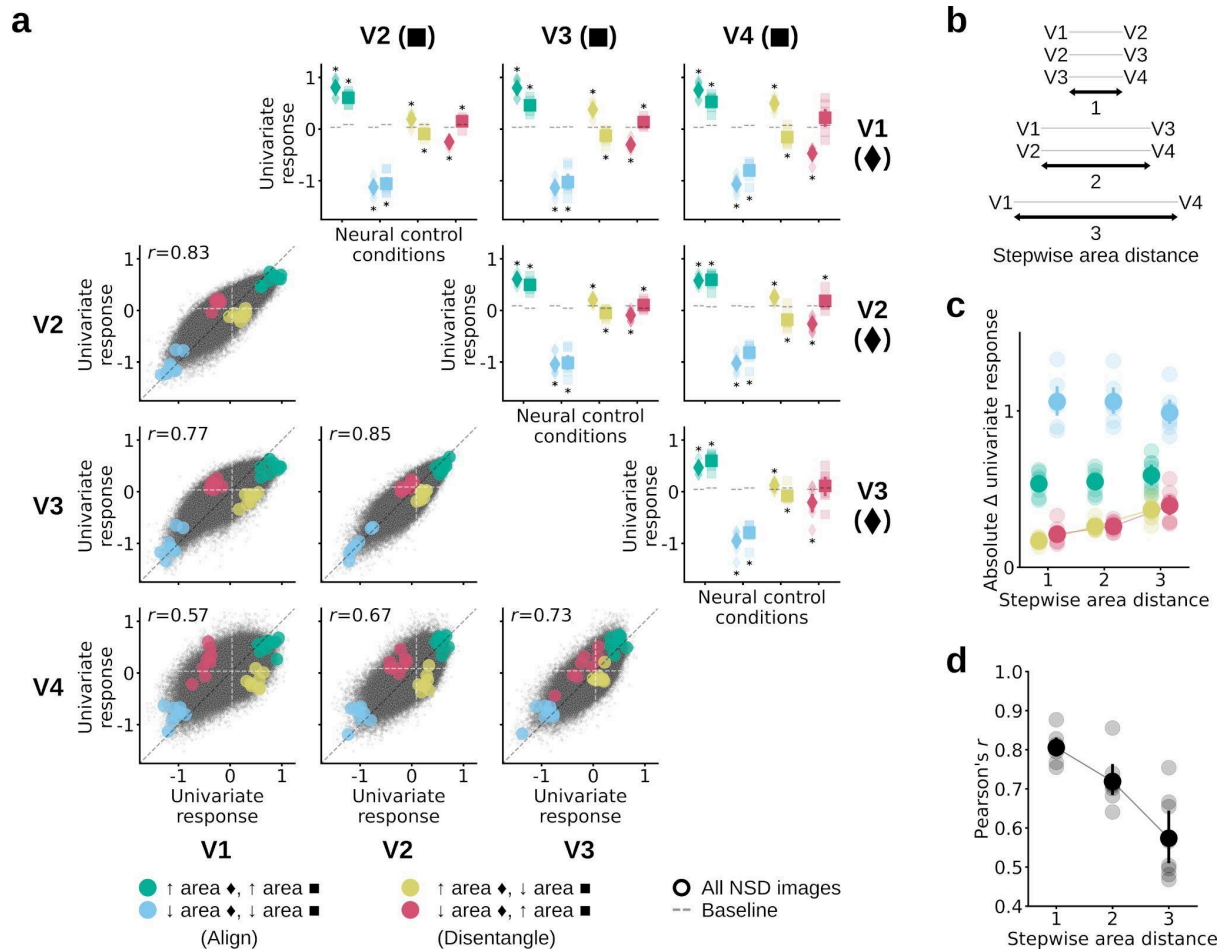
Supplementary Fig. 1 | Encoding models. **a**, Encoding model training. For each subject and area, we trained end-to-end encoding models that take images as input and predict the corresponding fMRI responses, using the single-trial NSD responses for the 9,000 subject-unique images. During training, the model predictions were compared to the single-trial target fMRI responses, and the resulting error was backpropagated to update the encoding model weights. **b**, We tested the encoding models on an independent portion of the NSD data not used for training, consisting of fMRI responses for 515 images seen three times by all subjects, averaged across the three trials. The encoding models achieved a subject-average explained variance score of 65.94% for V1, 59.71% for V2, 52.92% for V3, and 44.45% for V4. For individual subjects' explained variance scores see **Supplementary Fig. 2**. **c**, We compared the noise of the in silico fMRI responses with the noise of the in vivo fMRI responses from the NSD, by comparing how much variance these two data types explained for a third, independent split of the in vivo NSD responses. Because the in silico neural responses did not capture all signal variance in the NSD responses (**Supplementary Fig. 1b**), the in silico neural responses explaining more variance than the in vivo NSD responses would be indicative of the former being less affected by noise¹⁹. We carried out the comparison through three sets of predictions, using the in silico and the in vivo NSD fMRI responses for the 515 test images (**Supplementary Fig. 1b**). Each prediction involved explaining in vivo single NSD experiment response trials with a different predictor. In the first set of predictions, the predictor consisted of one of the two remaining in vivo NSD experiment response trials. In the second set of predictions, the predictor consisted of the average of the two remaining in vivo NSD experiment response trials. In the third set of predictions, the predictor consisted of the in silico responses from the trained encoding models. **d**, Single NSD response trials explained variance, for the three predictors of the noise analysis. The variance explained by the in silico responses is higher than the variance explained by both single and averaged NSD trials, indicating that the in silico neural responses are less affected by noise compared to the NSD responses. Colored asterisks indicate significant difference between the explained variance scores of two predictors ($p < 0.05$, paired-sample one-sided t -test, Benjamini/Hochberg corrected, $n = 8$ subjects), for each area. Error bars reflect 95% confidence intervals.



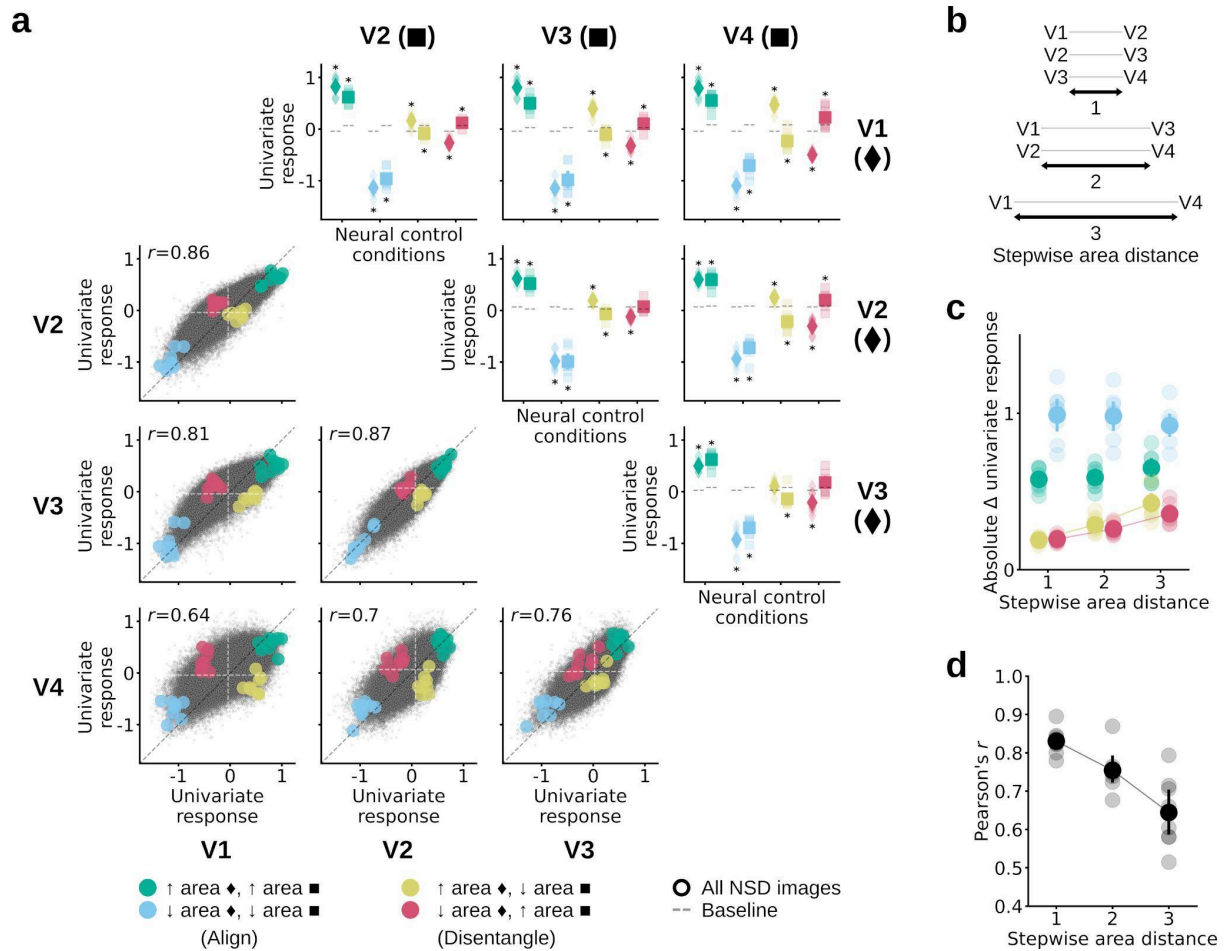
Supplementary Fig. 2 | Explained variance for the encoding models of each subject and visual area.



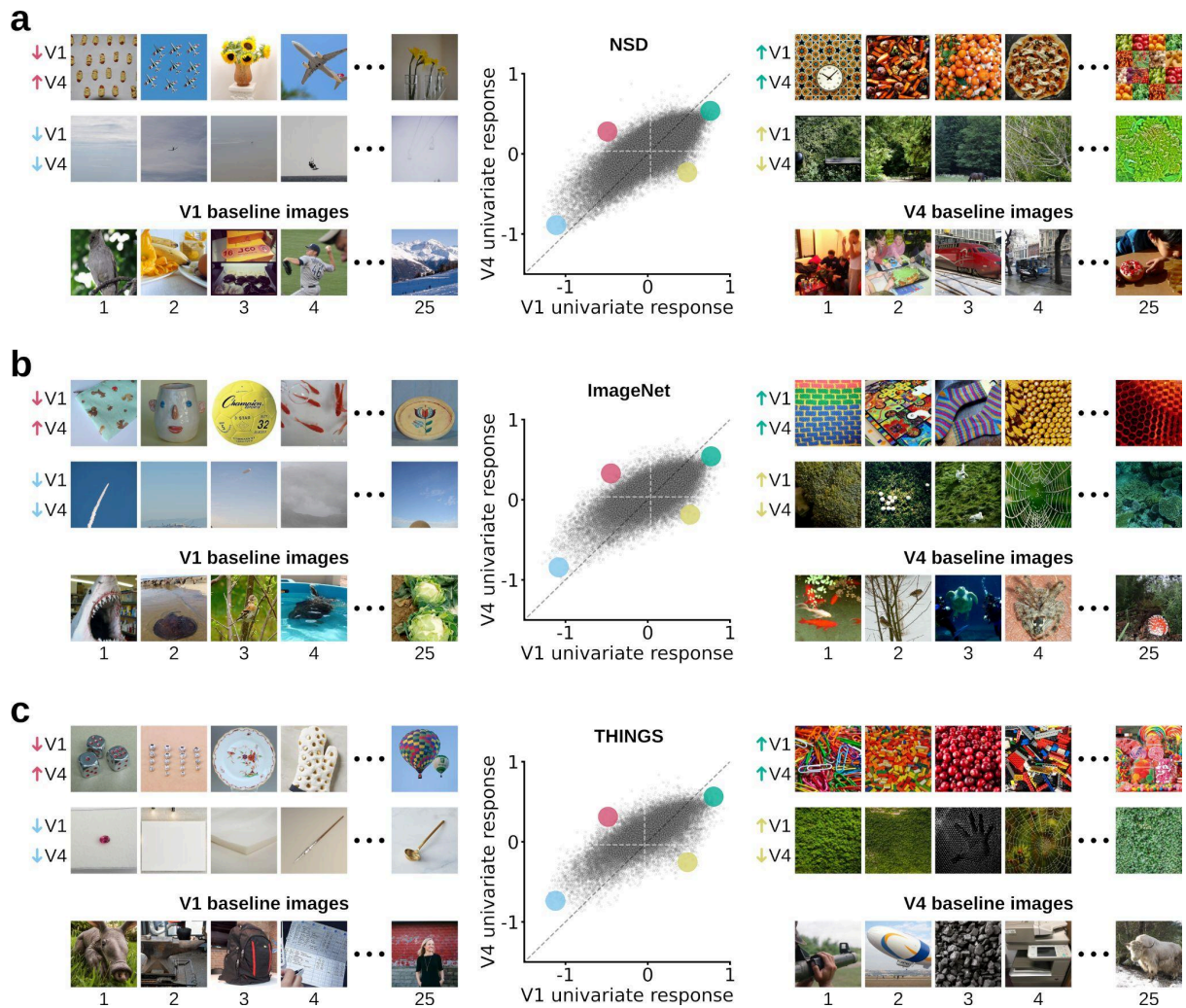
Supplementary Fig. 3 | Univariate RNC algorithm. Univariate RNC searches for images leading to aligned or disentangled in silico univariate fMRI responses of two visual areas. The 73,000 NSD images are fed to the trained encoding models of two areas, and the resulting in silico fMRI responses averaged across voxels, obtaining a one-dimensional univariate response vector of length 73,000, for each area. The univariate response vectors of the two areas are either summed (alignment) or subtracted (disentanglement), the sum/difference scores ranked, and the controlling images leading to highest and lowest scores are kept. This results in four sets of controlling images, each set corresponding to a different neural control condition. The controlling images from the sum vector lead to two neural control conditions in which both areas have aligned univariate responses (i.e., images that either drive or suppress the responses of both areas), whereas the controlling images from the difference vector lead to two neural control conditions in which both areas have disentangled univariate responses (i.e. images that drive the responses of one area while suppressing the responses of the other area, and vice versa).



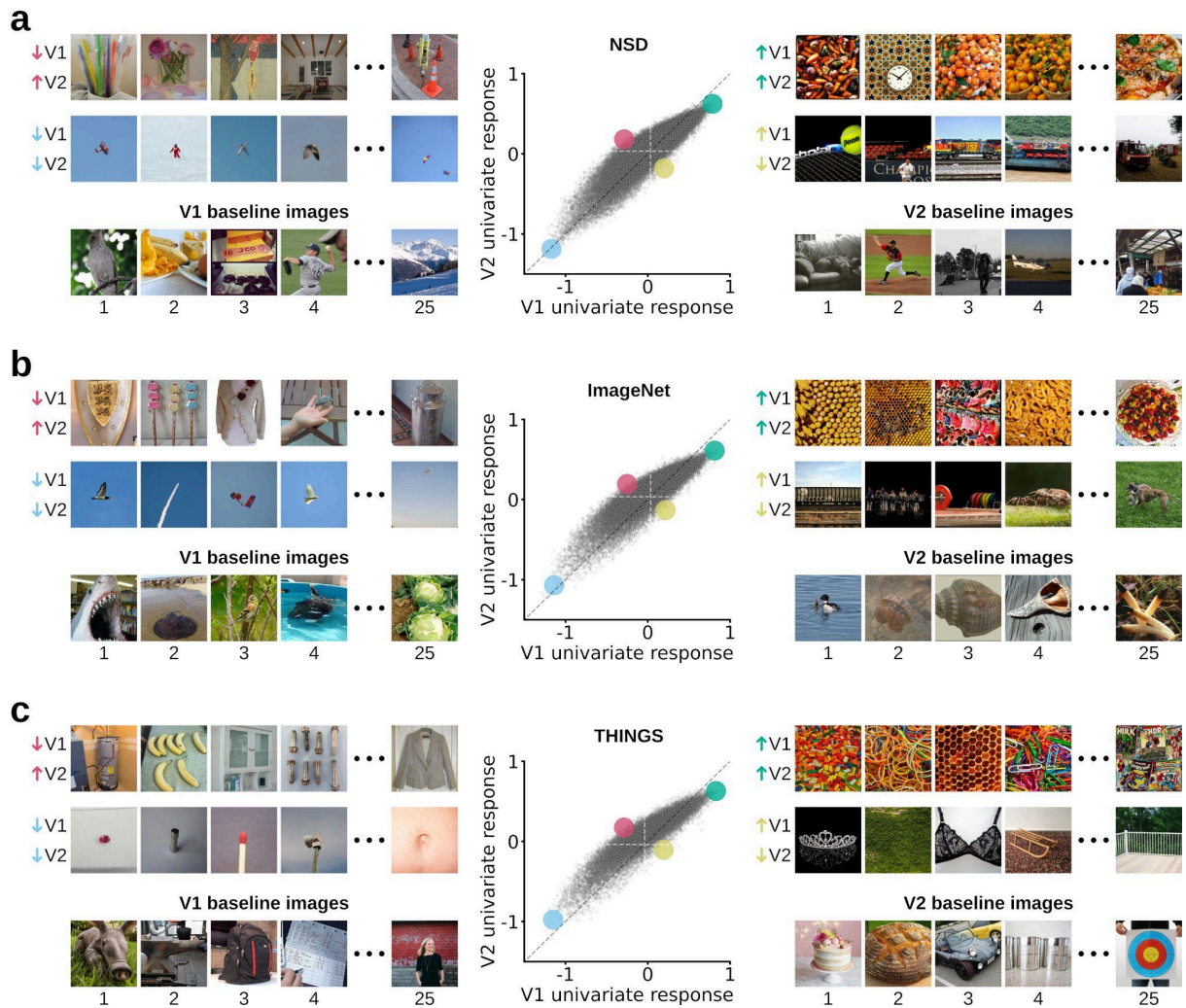
Supplementary Fig. 4 | Univariate RNC using the 50,000 ImageNet validation images, quantitative results. **a**, Univariate RNC results, embedded in a four-by-four matrix. **b**, Stepwise distance between areas. **c**, Absolute difference between controlling and baseline images univariate responses, averaged across all pairwise comparisons of areas with same stepwise distance. **d**, Correlation between the univariate responses of two areas, averaged across pairwise comparisons of areas with same stepwise distance.



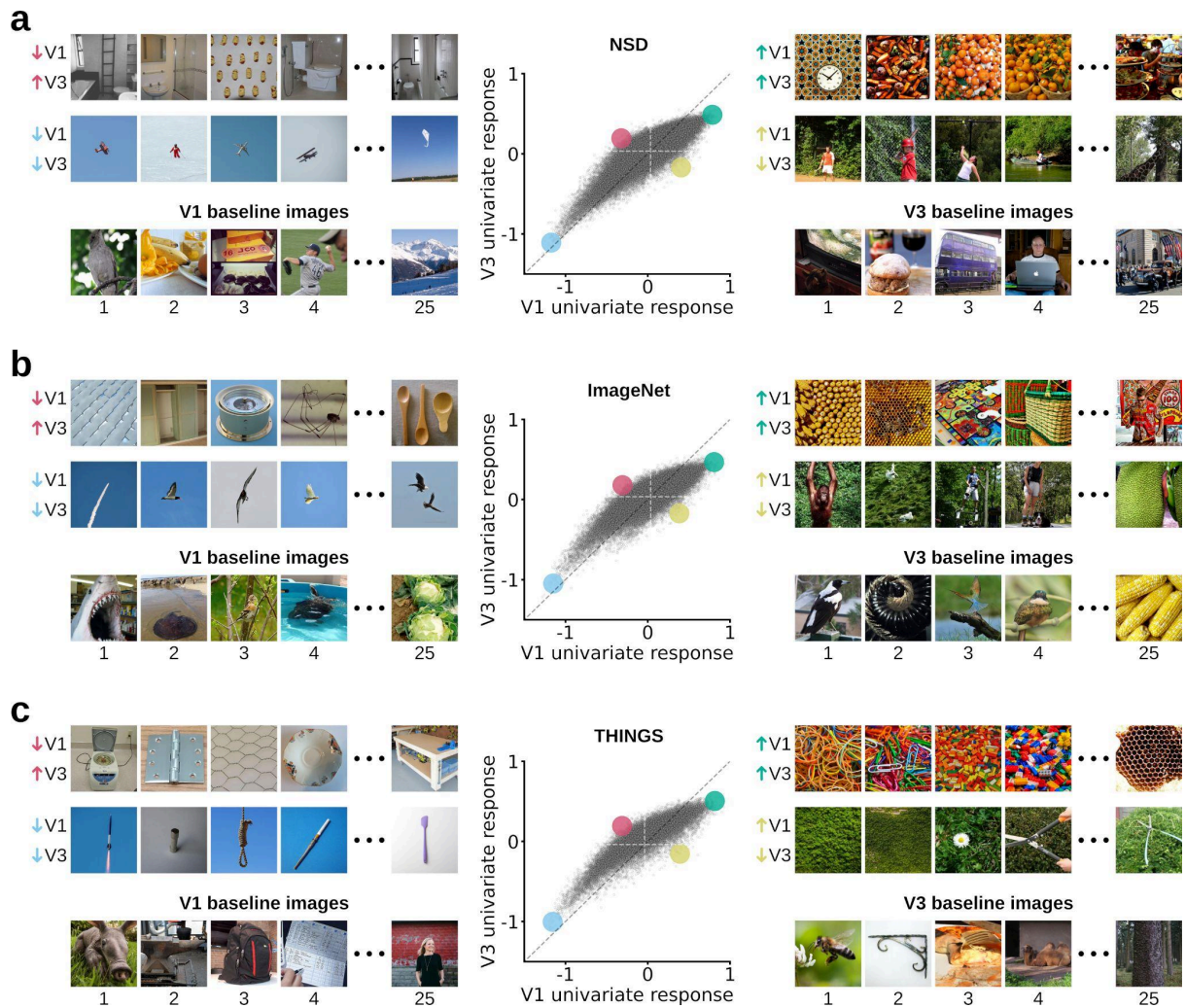
Supplementary Fig. 5 | Univariate RNC using the 26,107 THINGS images, quantitative results. a, Univariate RNC results, embedded in a four-by-four matrix. **b**, Stepwise distance between areas. **c**, Absolute difference between controlling and baseline images univariate responses, averaged across all pairwise comparisons of areas with same stepwise distance. **d**, Correlation between the univariate responses of two areas, averaged across pairwise comparisons of areas with same stepwise distance.



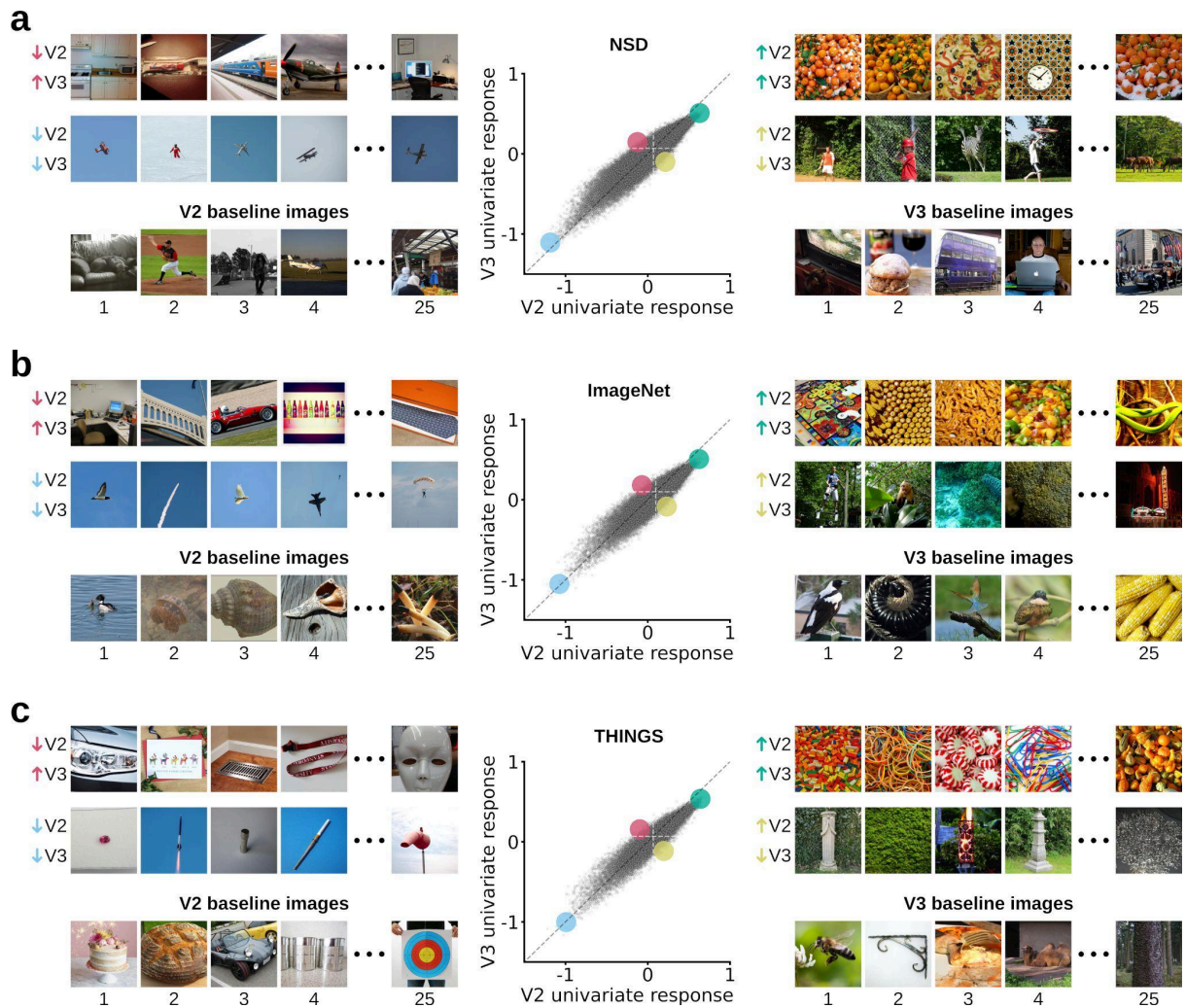
Supplementary Fig. 6 | Univariate RNC controlling and baseline images for the V1 vs. V4 comparison. **a**, Controlling and baseline images from univariate RNC applied on the in silico fMRI responses for the 73,000 NSD images. **b**, Controlling and baseline images from univariate RNC applied on the in silico fMRI responses for the 50,000 ImageNet validation images. **c**, Controlling and baseline images from univariate RNC applied on the in silico fMRI responses for the 26,107 THINGS images.



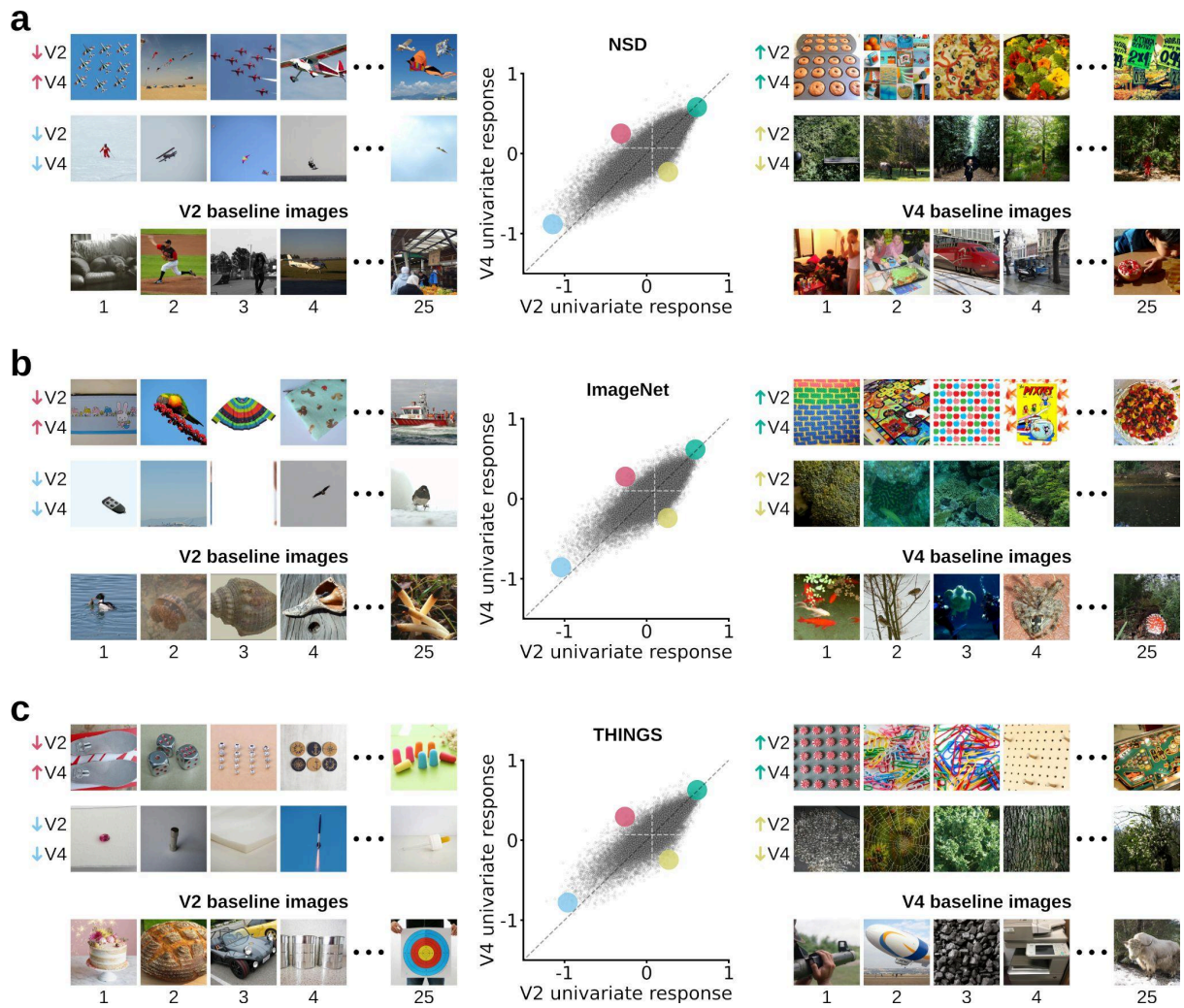
Supplementary Fig. 7 | Univariate RNC controlling and baseline images for the V1 vs. V2 comparison. **a**, Controlling and baseline images from univariate RNC applied on the in silico fMRI responses for the 73,000 NSD images. **b**, Controlling and baseline images from univariate RNC applied on the in silico fMRI responses for the 50,000 ImageNet validation images. **c**, Controlling and baseline images from univariate RNC applied on the in silico fMRI responses for the 26,107 THINGS images.



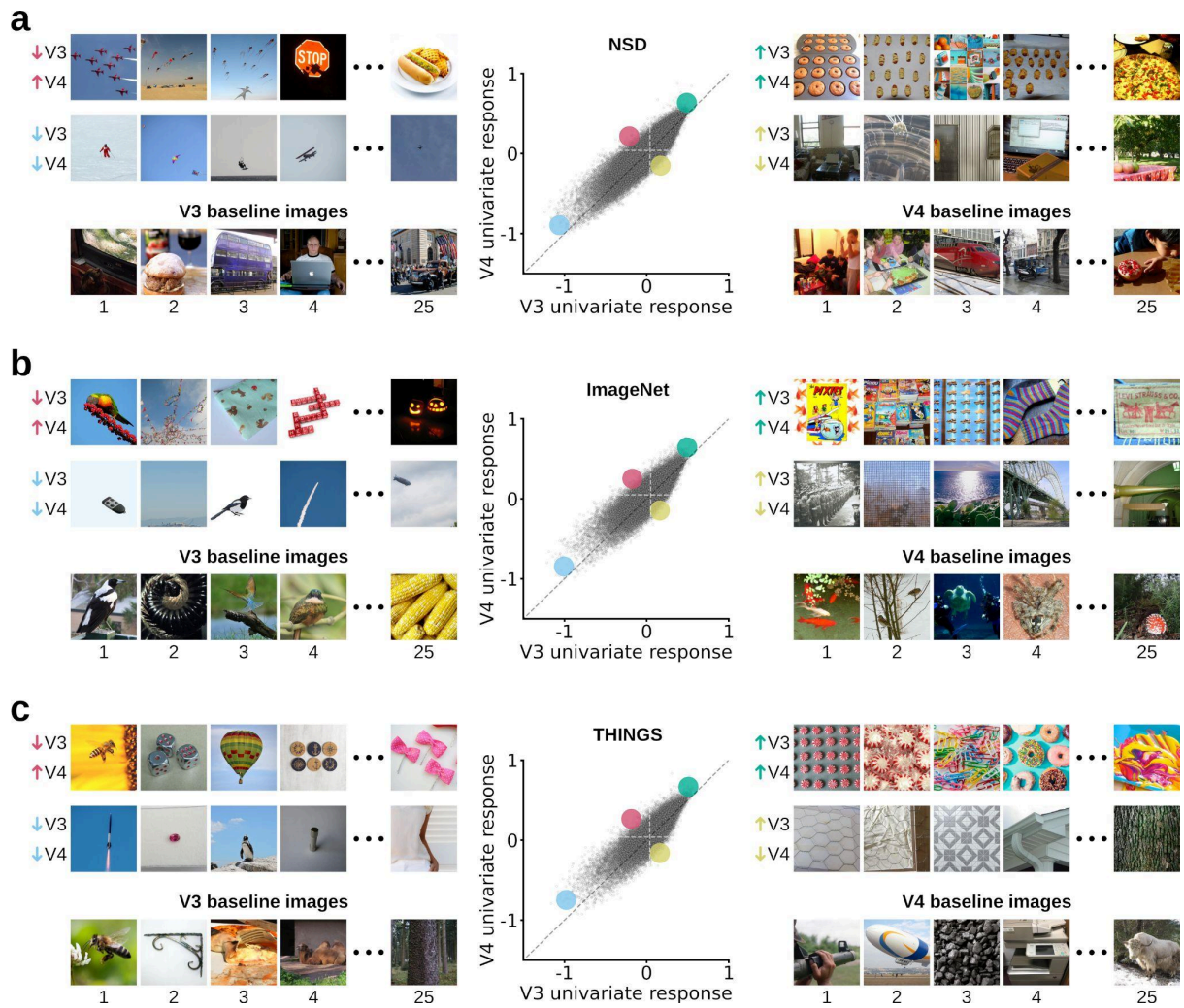
Supplementary Fig. 8 | Univariate RNC controlling and baseline images for the V1 vs. V3 comparison. **a**, Controlling and baseline images from univariate RNC applied on the in silico fMRI responses for the 73,000 NSD images. **b**, Controlling and baseline images from univariate RNC applied on the in silico fMRI responses for the 50,000 ImageNet validation images. **c**, Controlling and baseline images from univariate RNC applied on the in silico fMRI responses for the 26,107 THINGS images.



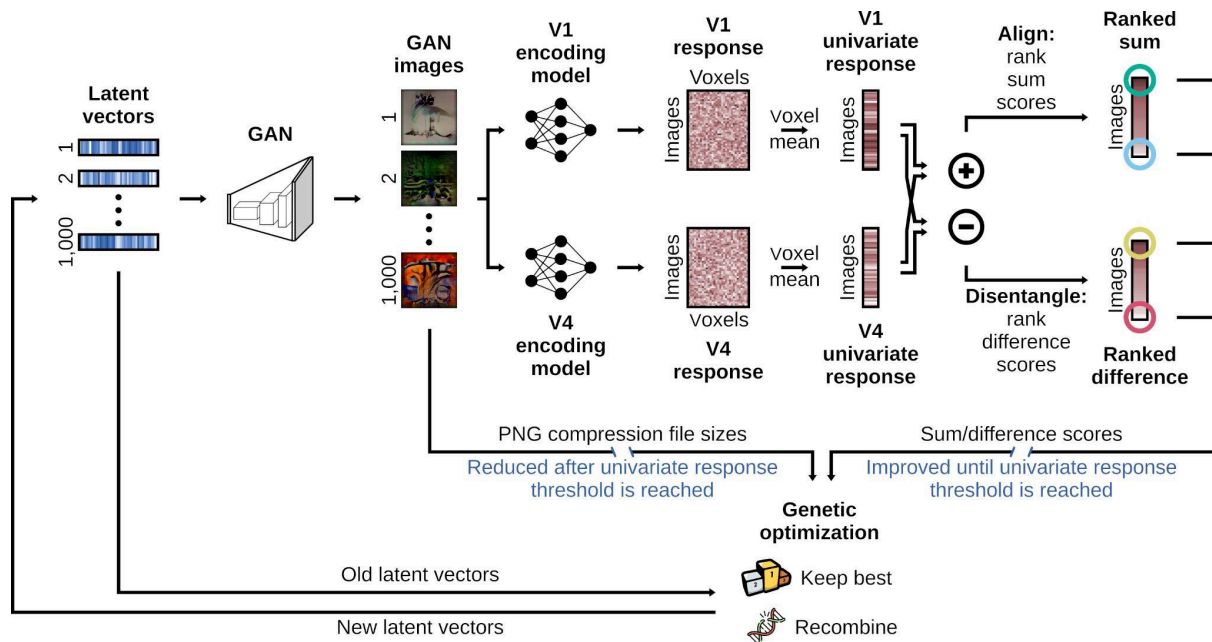
Supplementary Fig. 9 | Univariate RNC controlling and baseline images for the V2 vs. V3 comparison. **a**, Controlling and baseline images from univariate RNC applied on the in silico fMRI responses for the 73,000 NSD images. **b**, Controlling and baseline images from univariate RNC applied on the in silico fMRI responses for the 50,000 ImageNet validation images. **c**, Controlling and baseline images from univariate RNC applied on the in silico fMRI responses for the 26,107 THINGS images.



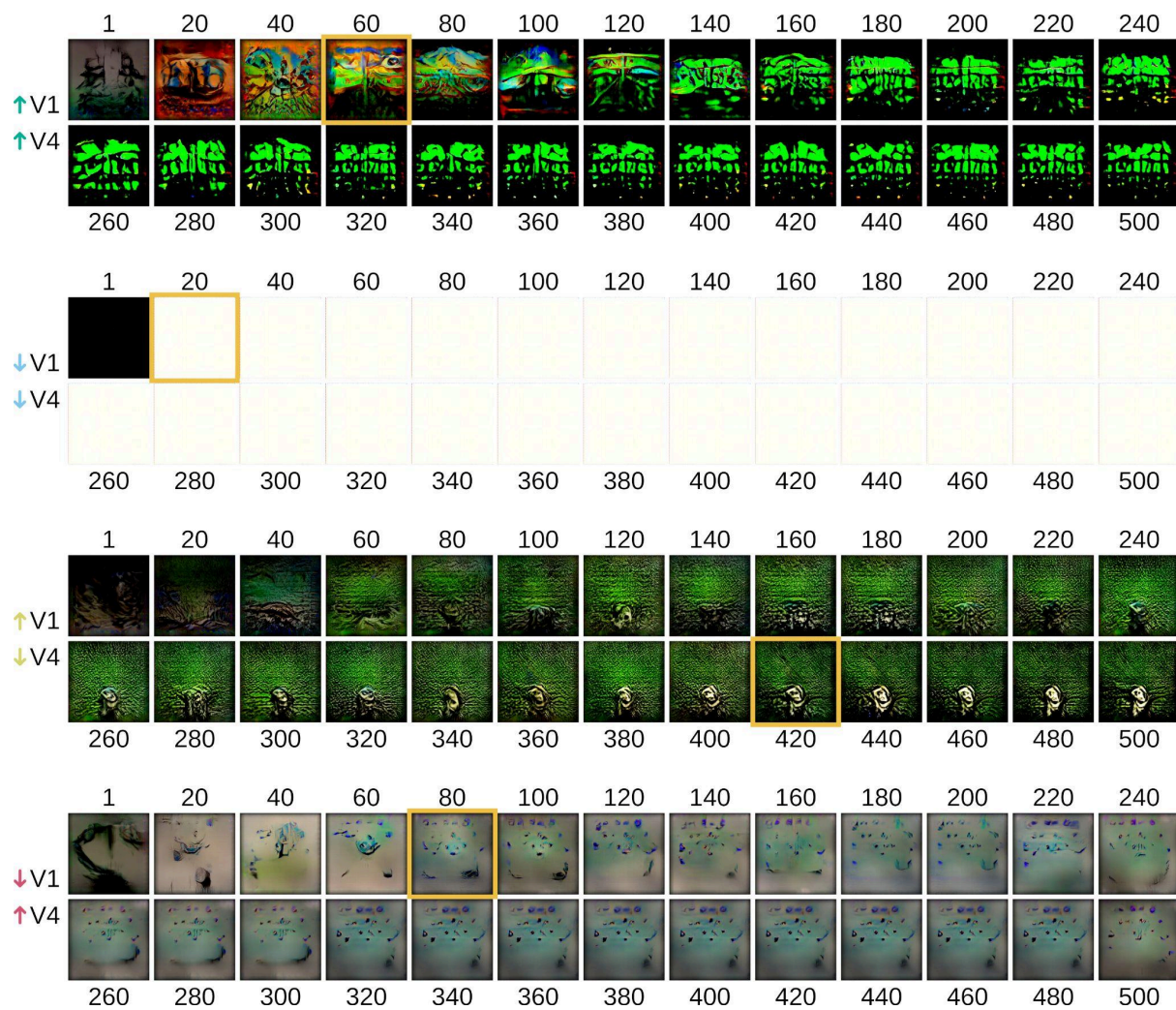
Supplementary Fig. 10 | Univariate RNC controlling and baseline images for the V2 vs. V4 comparison. **a**, Controlling and baseline images from univariate RNC applied on the in silico fMRI responses for the 73,000 NSD images. **b**, Controlling and baseline images from univariate RNC applied on the in silico fMRI responses for the 50,000 ImageNet validation images. **c**, Controlling and baseline images from univariate RNC applied on the in silico fMRI responses for the 26,107 THINGS images.



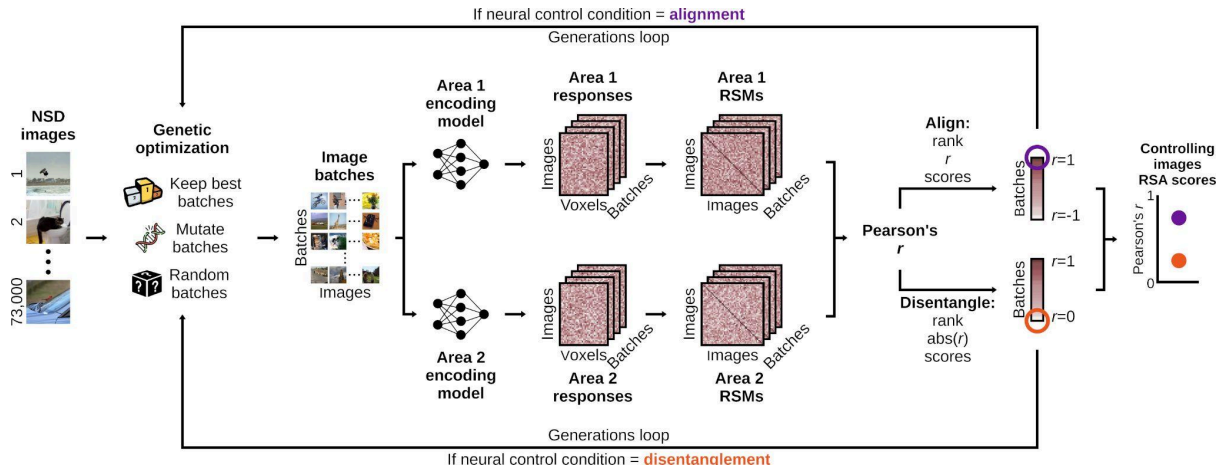
Supplementary Fig. 11 | Univariate RNC controlling and baseline images for the V3 vs. V4 comparison. **a**, Controlling and baseline images from univariate RNC applied on the in silico fMRI responses for the 73,000 NSD images. **b**, Controlling and baseline images from univariate RNC applied on the in silico fMRI responses for the 50,000 ImageNet validation images. **c**, Controlling and baseline images from univariate RNC applied on the in silico fMRI responses for the 26,107 THINGS images.



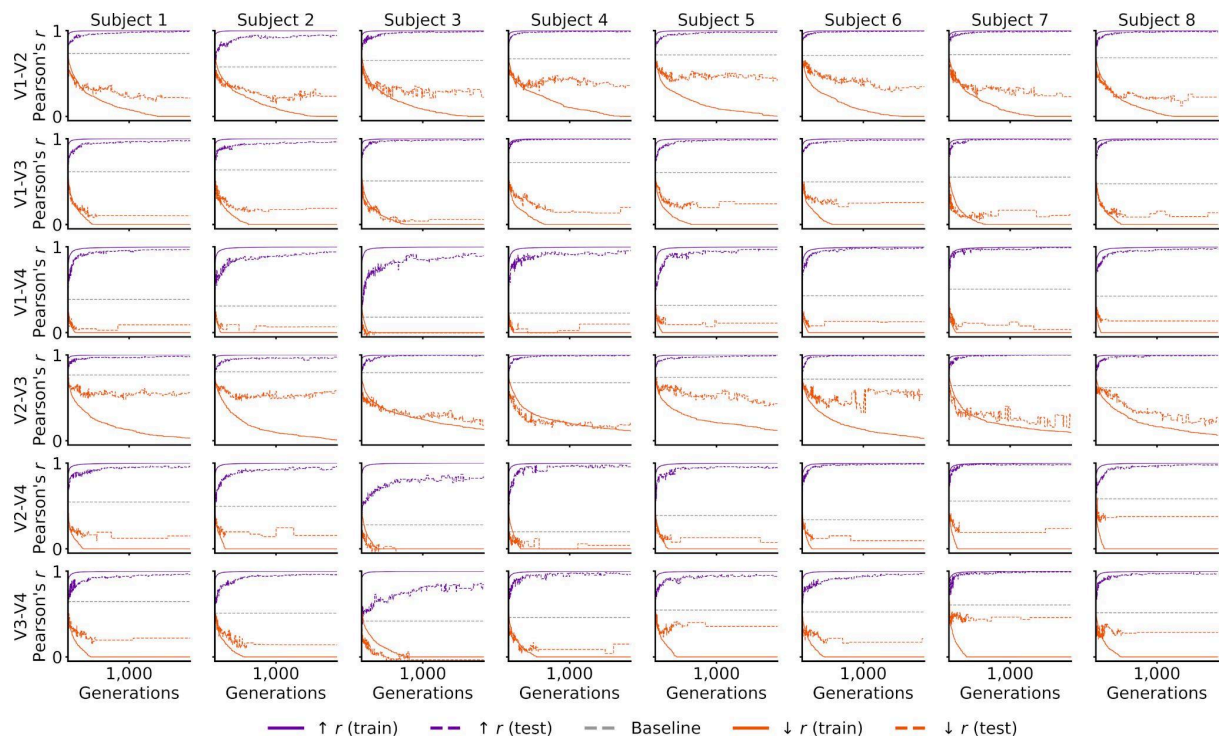
Supplementary Fig. 12 | Generative univariate RNC algorithm. Generative univariate RNC generates stimulus images leading to aligned or disentangled in silico univariate fMRI responses for V1 and V4, while at the same time being as simple as possible. A batch of 1,000 random latent vectors is given as input to a GAN³⁴, which uses them to generate 1,000 images, and the PNG compression file size of these images is calculated. Next, these images are fed to the trained encoding models of V1 and V4, and the resulting in silico fMRI responses averaged across voxels, obtaining a one-dimensional univariate response vector of length 1,000, for each area. The univariate response vectors of the two areas are either summed or subtracted, based on the neural control condition univariate RNC is optimizing for, thus obtaining sum/difference scores. The latent vectors, PNG compression file sizes, univariate responses, and sum/difference scores are then fed to a genetic optimization algorithm^{35,36}, which uses them to create a new generation of latent vectors (by keeping the 250 best performing latent vectors, and recombining the remaining 750 latent vectors). At first the latent vectors are optimized using the sum/difference scores, so to result in images leading to in silico univariate fMRI responses for V1 and V4 closer to a threshold level. After this threshold is reached, the latent vectors are optimized using the PNG compression file sizes, so to result in images that are as simple as possible (while keeping the in silico univariate fMRI responses over the threshold). Finally, the new latent vectors are once again fed to the GAN, and the same steps are repeated over a new generation. After several genetic algorithm optimizations, this results in an image (i.e., the best performing image from the last genetic optimization generation) that well controls neural responses following one of the four univariate RNC neural control conditions (i.e., two alignment conditions where the in silico univariate fMRI responses of both areas are either driven or suppressed, and two disentanglement conditions where the in silico univariate fMRI response of one area is driven while the response of the other area is suppressed, and vice versa), while at the same time being as simple as possible. The images for the four neural control conditions are optimized independently of each other.



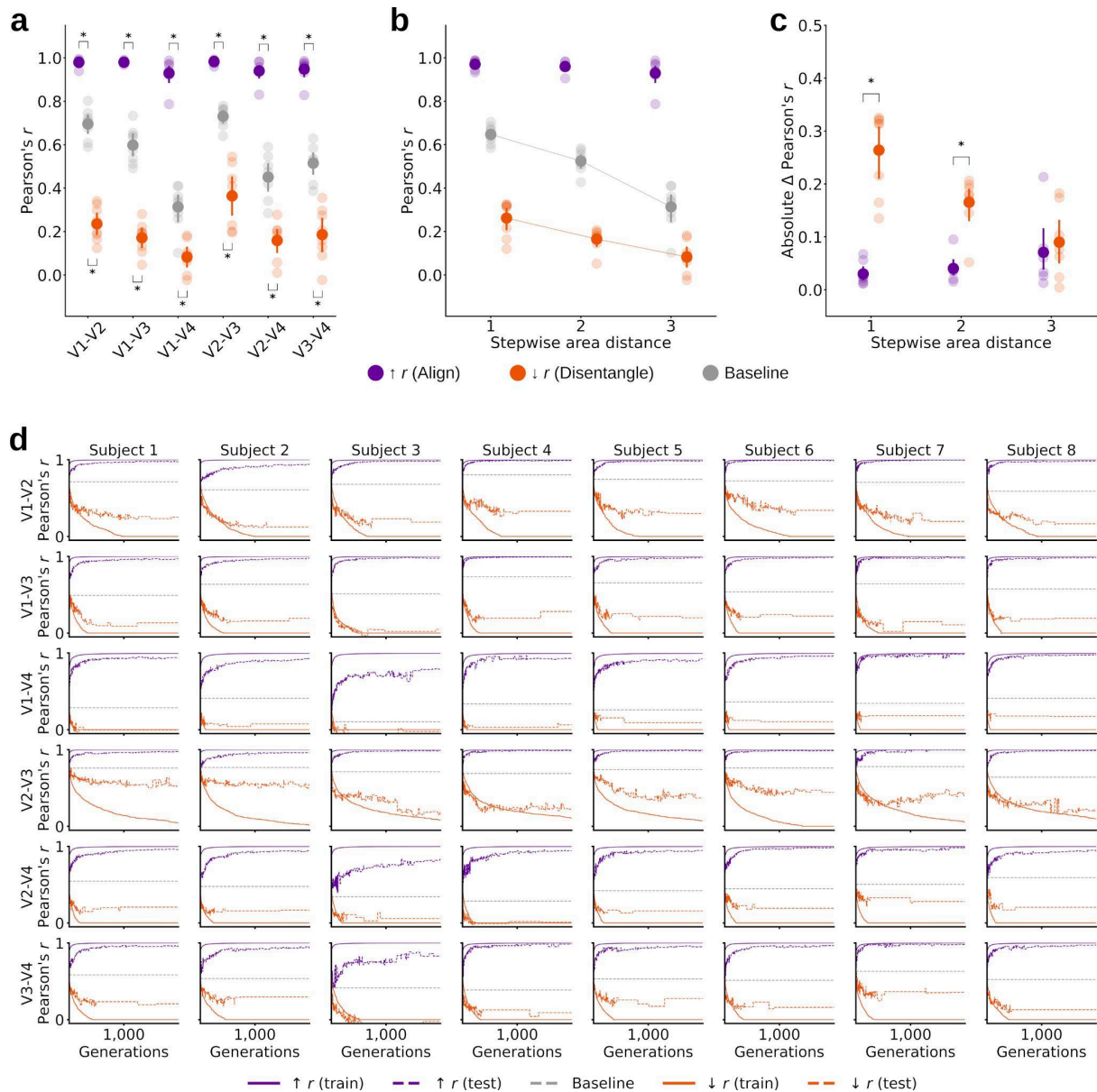
Supplementary Fig. 13 | Generative univariate RNC image solutions across generations. For each neural control condition, the generated images from the 500 genetic optimization generations are shown in intervals of 20 generations. Generation numbers are added above or below the images. Only the best performing image from each generation is displayed (out of all 1,000 images tested in each generation). The images are optimized to control univariate responses up to a threshold, after which they are optimized to reduce their PNG compression file sizes. The univariate response threshold is reached at generation 41 for the neural control condition driving both V1 and V4, at generation 13 for the neural control condition suppressing both V1 and V4, at generation 402 for the neural control condition driving V1 while suppressing V4, and at generation 73 for the neural control condition suppressing V1 while driving V4. For each neural control condition, the first post-threshold generation image is surrounded by a golden box.



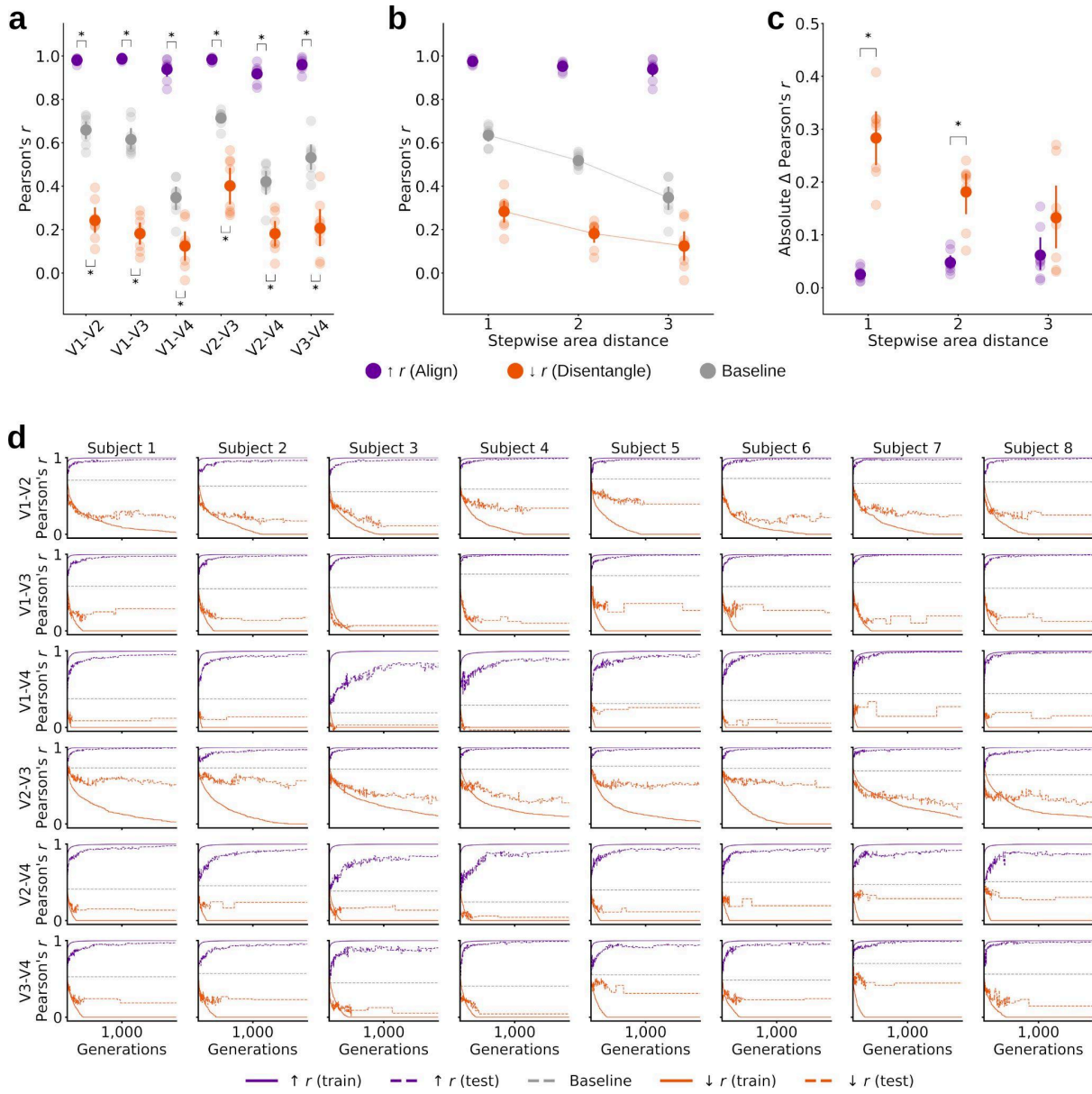
Supplementary Fig. 14 | Multivariate RNC algorithm. Multivariate RNC searches for images leading to aligned or disentangled in silico multivariate fMRI responses of two visual brain areas. Random images batches from the 73,000 NSD images are fed to the trained encoding models of two areas, and the resulting in silico fMRI responses are transformed into representational similarity matrices (RSMs)²⁵, yielding one RSM for each image batch and area. The RSMs of the two areas are then compared through RSA (i.e., Pearson's correlation), obtaining one RSA correlation score (r) for each image batch, and the correlation scores ranked. To align the two areas, the image batches with highest correlation scores (i.e., containing images most similarly represented by the two areas) undergo a genetic optimization^{35,36,39,40} (which involves keeping these image batches, creating mutated versions of them, and adding random image batches), resulting in new image batches likely to better align the two areas. Finally, these new image batches are once again fed to the encoding models, and the same steps are repeated over a new generation. To disentangle the two areas the image batches with lowest absolute correlation scores (i.e., containing images most differently represented by the two areas) are instead genetically optimized, resulting in new image batches likely to better disentangle the two areas. After several genetic optimization generations, this results in an image batch that well controls neural responses following one of the two multivariate RNC neural control conditions. The controlling images from the ranked correlation vector lead both areas to have aligned multivariate responses (i.e., images leading to high RSA correlation scores for the two areas), whereas the controlling images from the absolute ranked correlation vector lead both areas to have disentangled multivariate responses (i.e., images leading to low absolute RSA correlation scores for the two areas). The image batches from the two neural control conditions are optimized independently of each other.



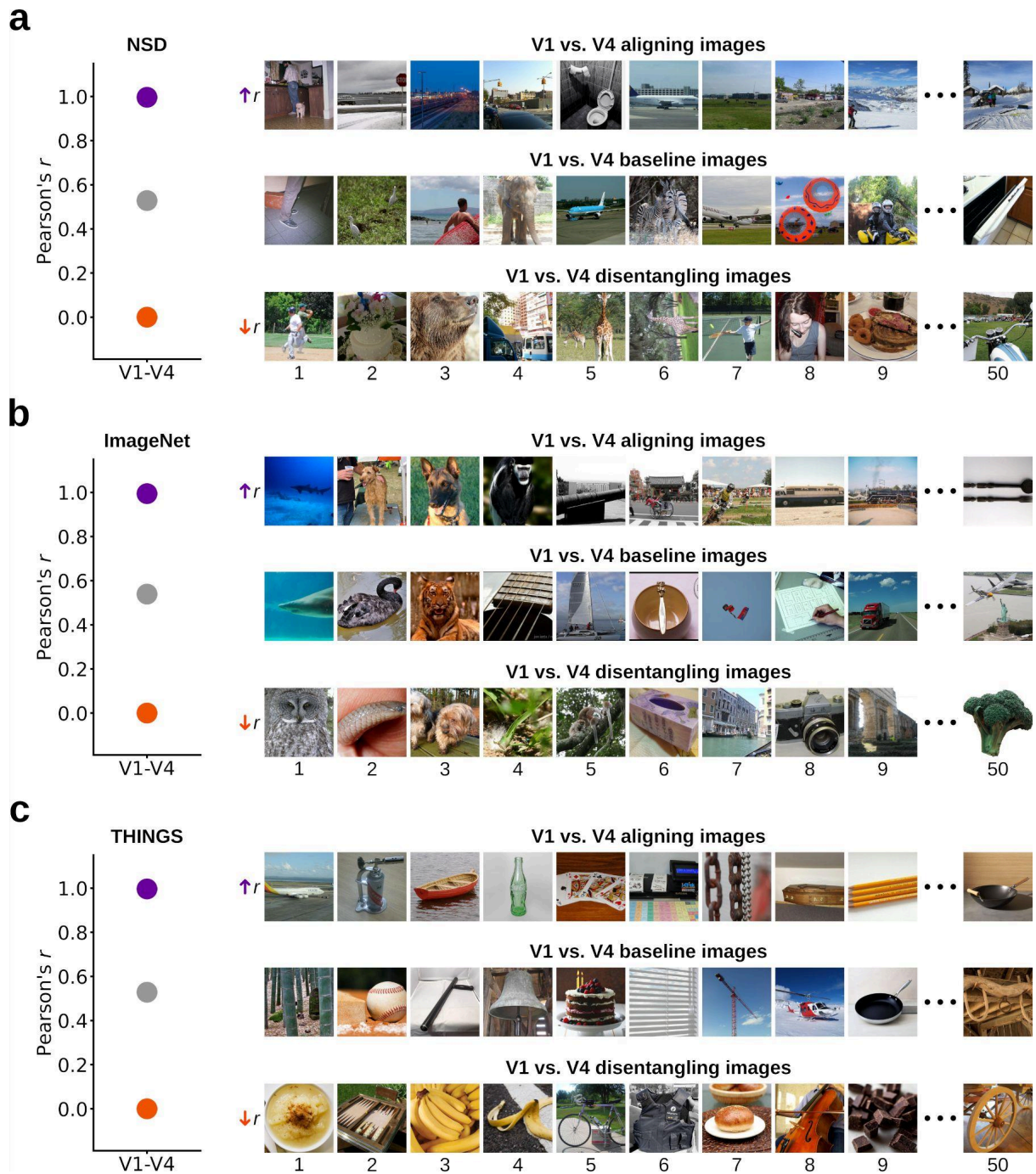
Supplementary Fig. 15 | Multivariate RNC optimization curves. Optimization curves of multivariate RNC applied on the in silico fMRI responses for the 73,000 NSD images. Each row corresponds to a different pairwise comparison of areas, and each column to a different subject. The train curves indicate the neural control condition scores for the subject-average RSMs on which multivariate RNC was applied, and the test curves indicate the neural control condition scores for the remaining subject on which the multivariate RNC solutions were cross-validated.



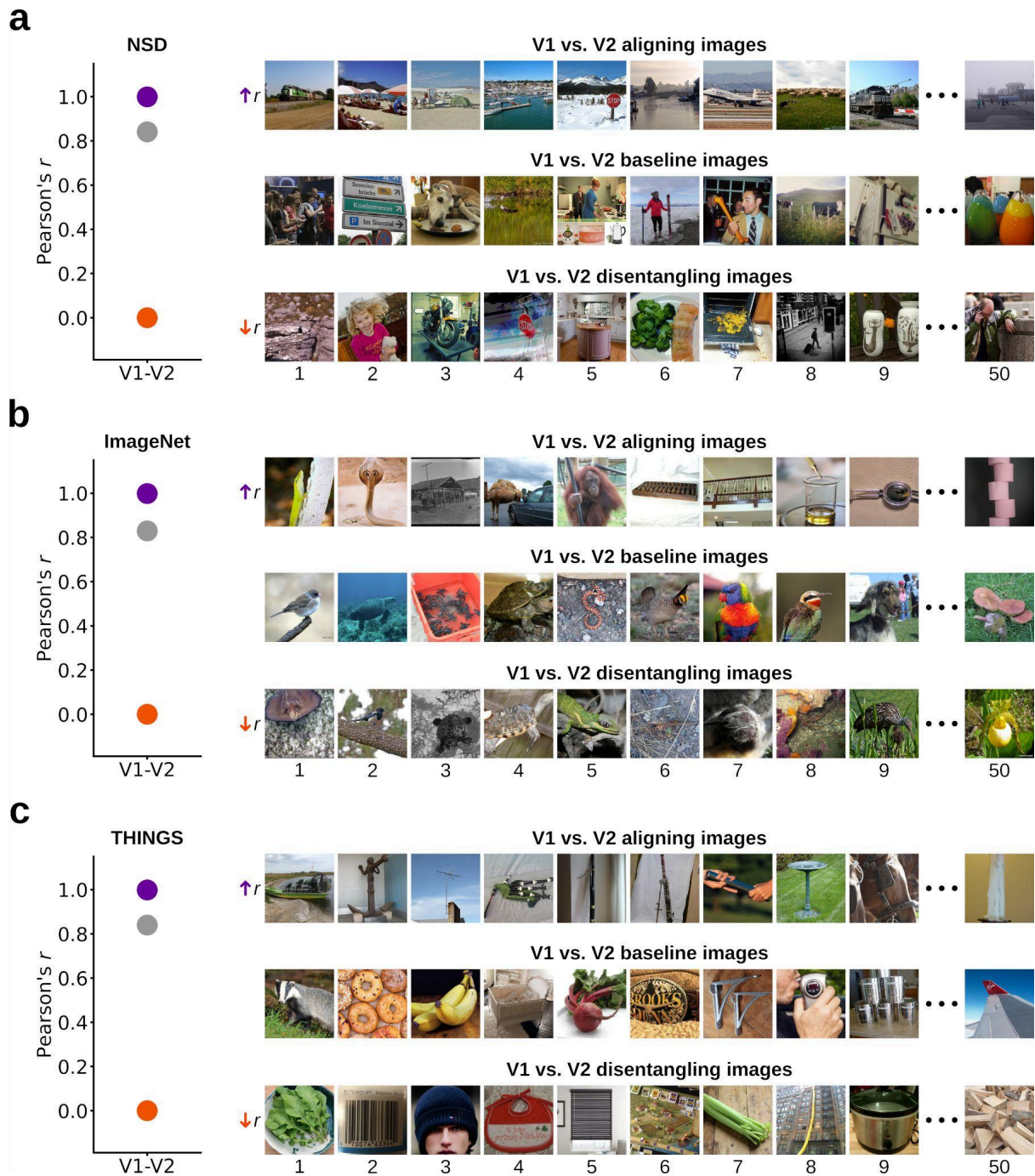
Supplementary Fig. 16 | Multivariate RNC using the 50,000 ImageNet validation images, quantitative results. **a**, Multivariate RNC results. **b**, Multivariate RNC RSA scores, averaged across pairwise comparisons of areas with same stepwise distance. **c**, Absolute Pearson's r difference between the observed multivariate RNC RSA scores and the target RSA scores (i.e., $r = 1$ for the alignment neural control condition, and $r = 0$ for the disentanglement neural control condition), averaged across pairwise comparisons of areas with same stepwise distance. **d**, Multivariate RNC optimization curves.



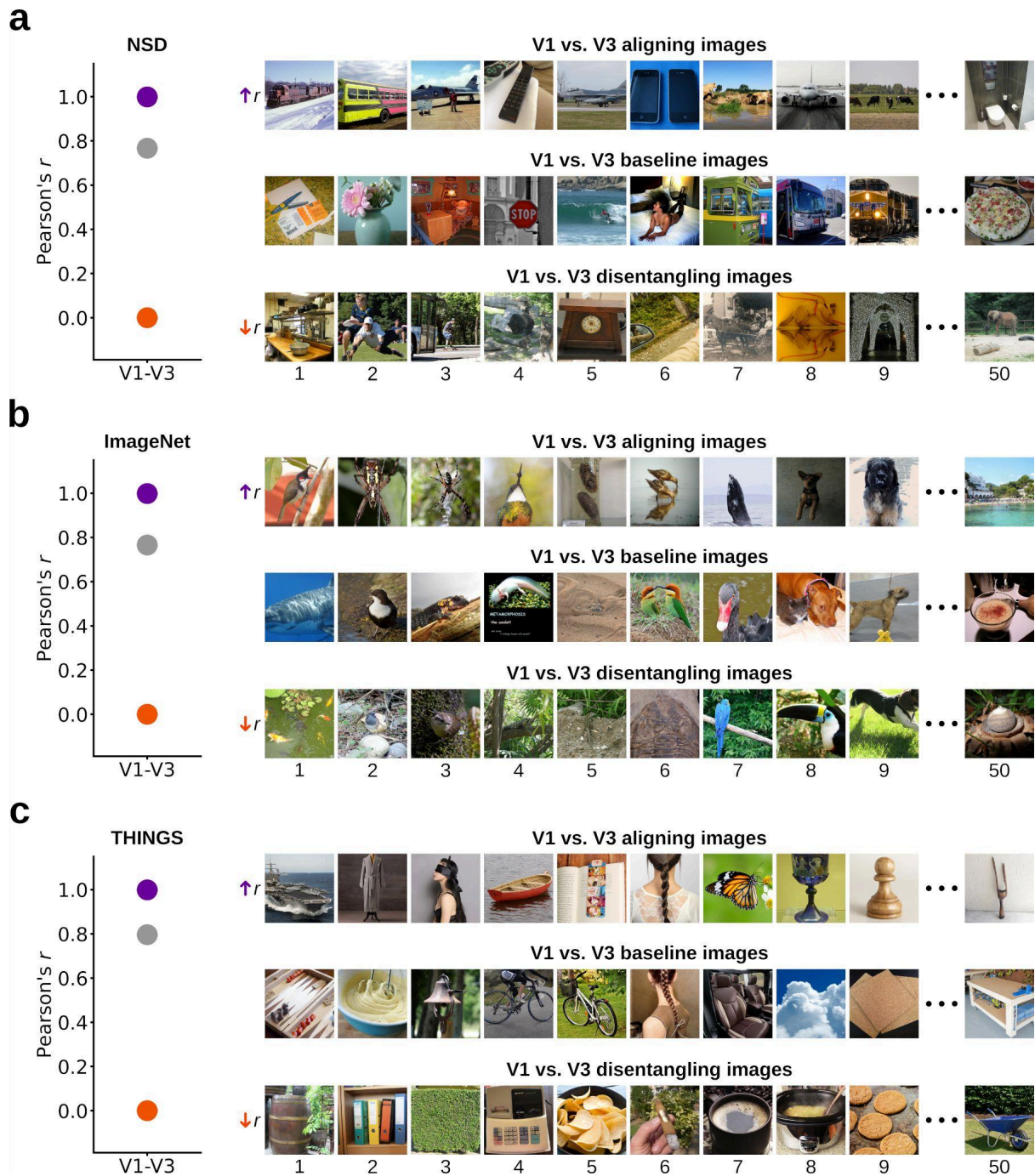
Supplementary Fig. 17 | Multivariate RNC using the 26,107 THINGS images, quantitative results.
a, Multivariate RNC results. **b**, Multivariate RNC RSA scores, averaged across pairwise comparisons of areas with same stepwise distance. **c**, Absolute Pearson's r difference between the observed multivariate RNC RSA scores and the target RSA scores (i.e., $r = 1$ for the alignment neural control condition, and $r = 0$ for the disentanglement neural control condition), averaged across pairwise comparisons of areas with same stepwise distance. **d**, Multivariate RNC optimization curves.



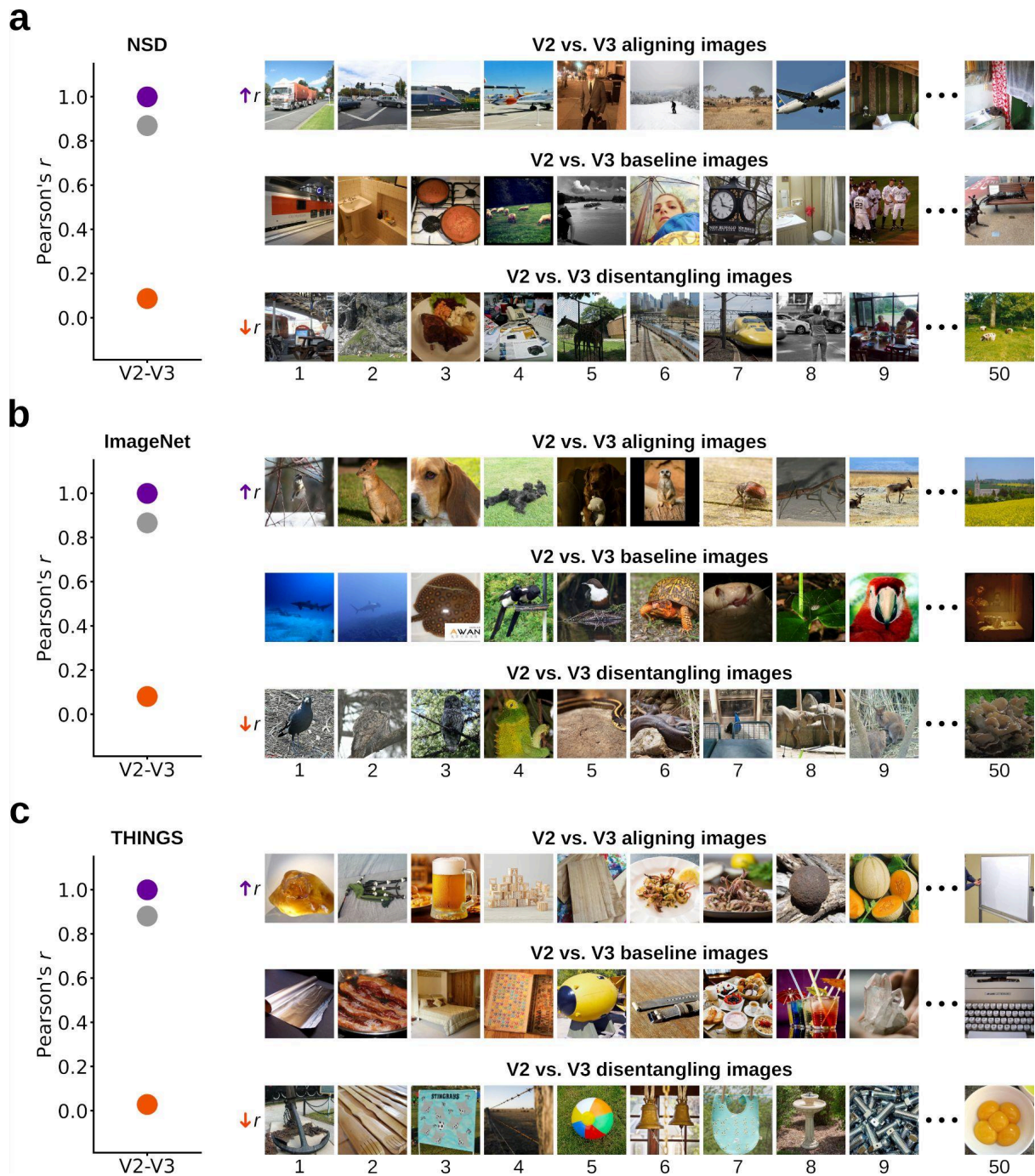
Supplementary Fig. 18 | Multivariate RNC controlling and baseline images for the V1 vs. V4 comparison. **a**, Controlling and baseline images from multivariate RNC applied on the in silico fMRI responses for the 73,000 NSD images. **b**, Controlling and baseline images from multivariate RNC applied on the in silico fMRI responses for the 50,000 ImageNet validation images. **c**, Controlling and baseline images from multivariate RNC applied on the in silico fMRI responses for the 26,107 THINGS images.



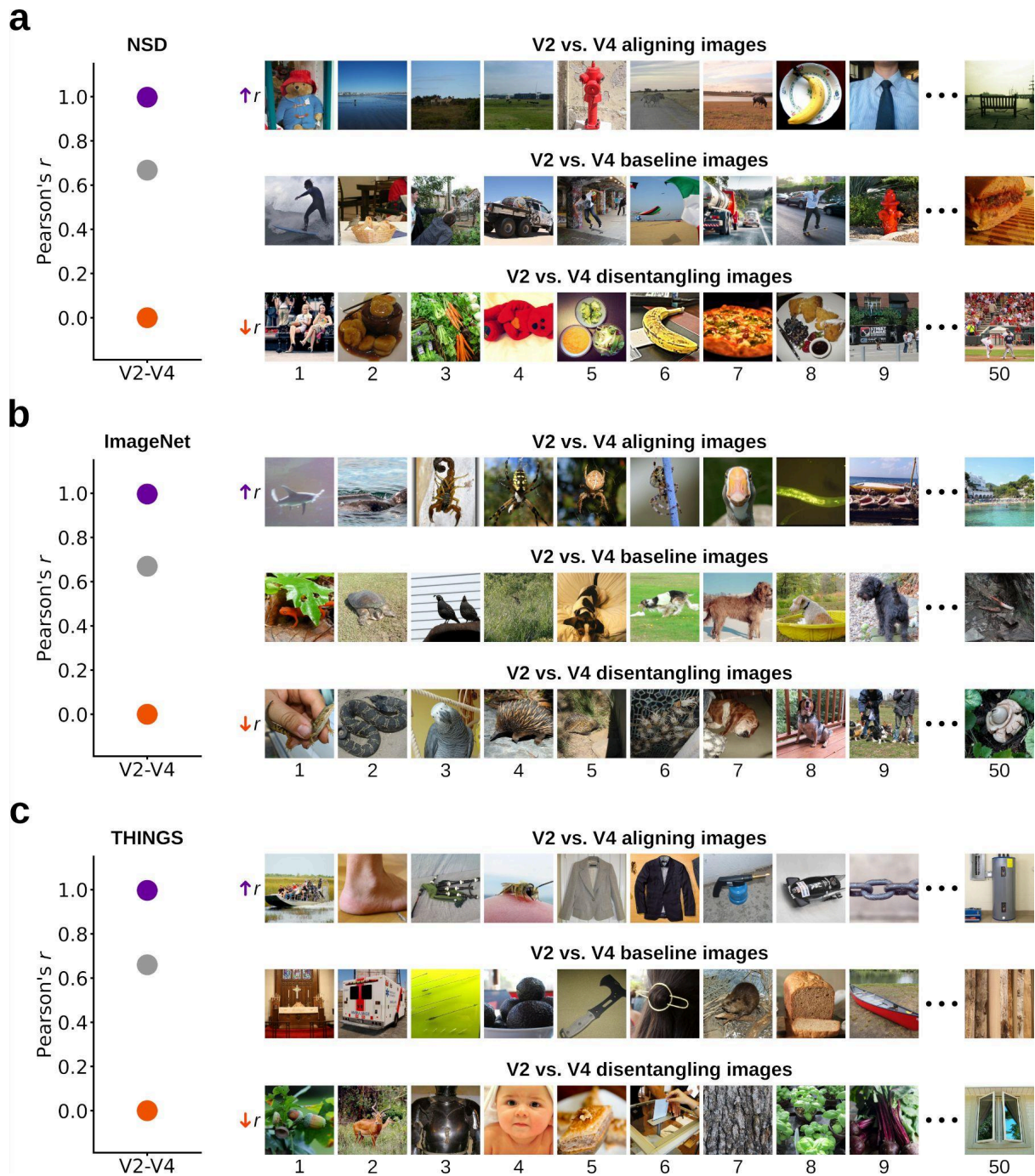
Supplementary Fig. 19 | Multivariate RNC controlling and baseline images for the V1 vs. V2 comparison. a, Controlling and baseline images from multivariate RNC applied on the in silico fMRI responses for the 73,000 NSD images. **b**, Controlling and baseline images from multivariate RNC applied on the in silico fMRI responses for the 50,000 ImageNet validation images. **c**, Controlling and baseline images from multivariate RNC applied on the in silico fMRI responses for the 26,107 THINGS images.



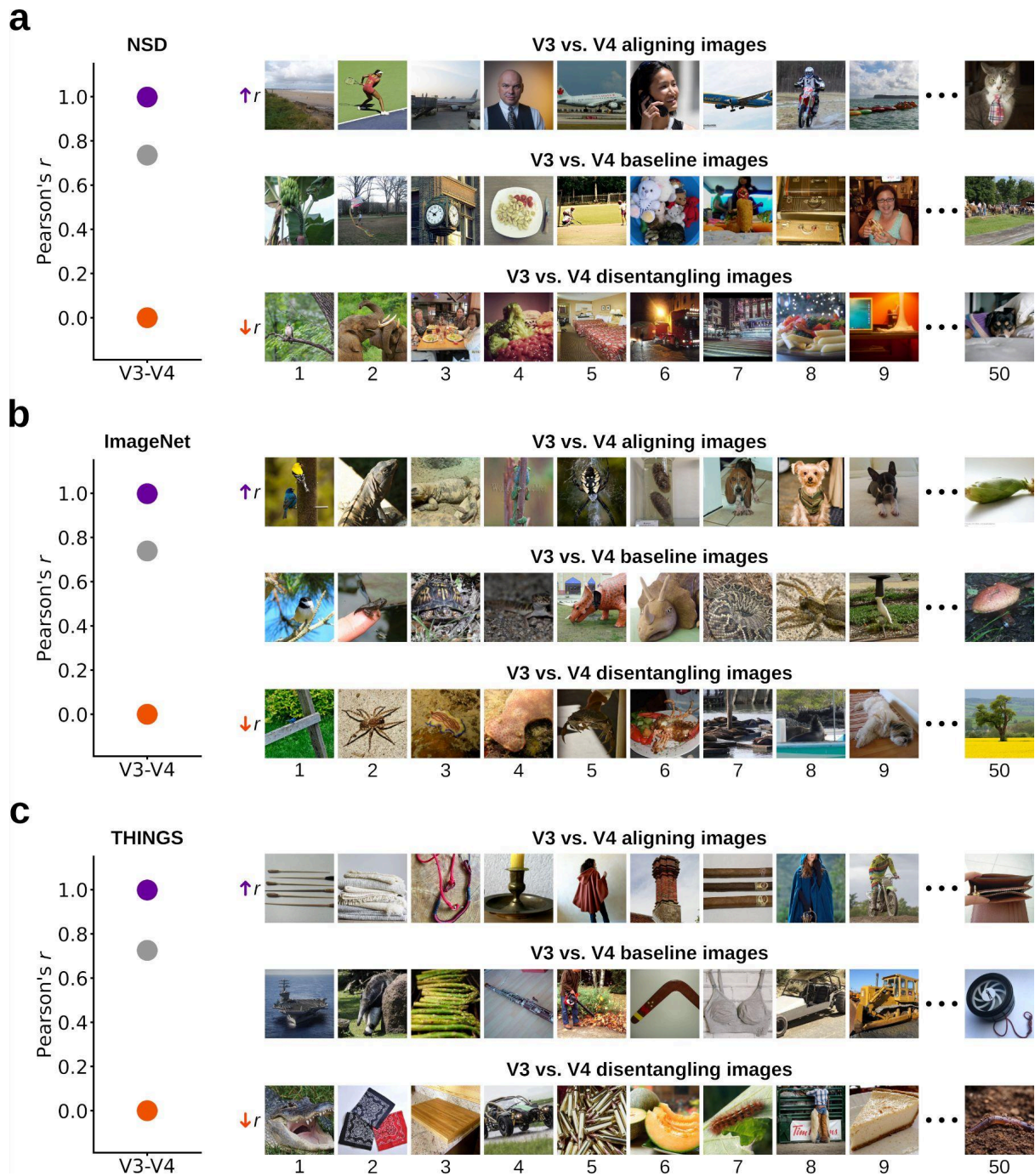
Supplementary Fig. 20 | Multivariate RNC controlling and baseline images for the V1 vs. V3 comparison. **a**, Controlling and baseline images from multivariate RNC applied on the in silico fMRI responses for the 73,000 NSD images. **b**, Controlling and baseline images from multivariate RNC applied on the in silico fMRI responses for the 50,000 ImageNet validation images. **c**, Controlling and baseline images from multivariate RNC applied on the in silico fMRI responses for the 26,107 THINGS images.



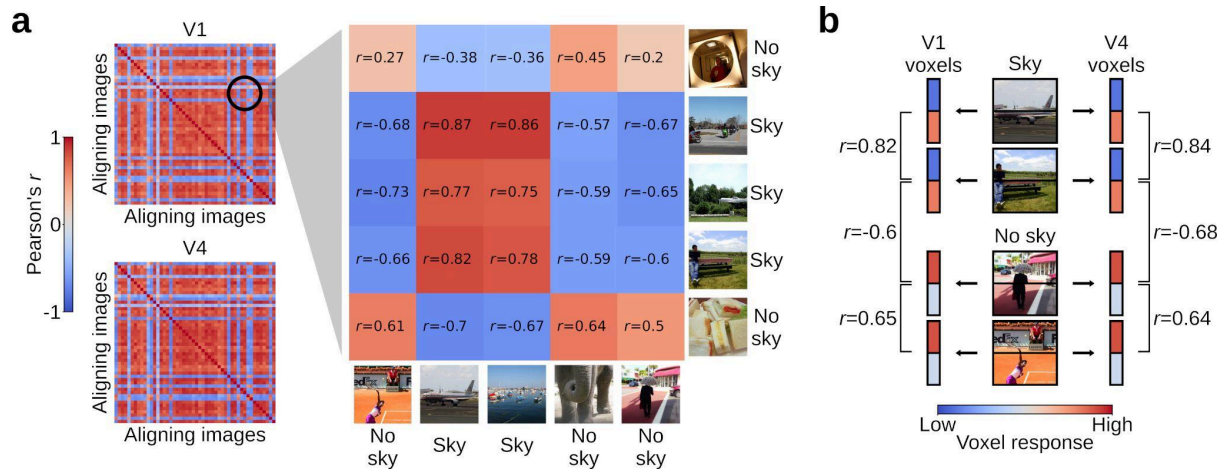
Supplementary Fig. 21 | Multivariate RNC controlling and baseline images for the V2 vs. V3 comparison. **a**, Controlling and baseline images from multivariate RNC applied on the in silico fMRI responses for the 73,000 NSD images. **b**, Controlling and baseline images from multivariate RNC applied on the in silico fMRI responses for the 50,000 ImageNet validation images. **c**, Controlling and baseline images from multivariate RNC applied on the in silico fMRI responses for the 26,107 THINGS images.



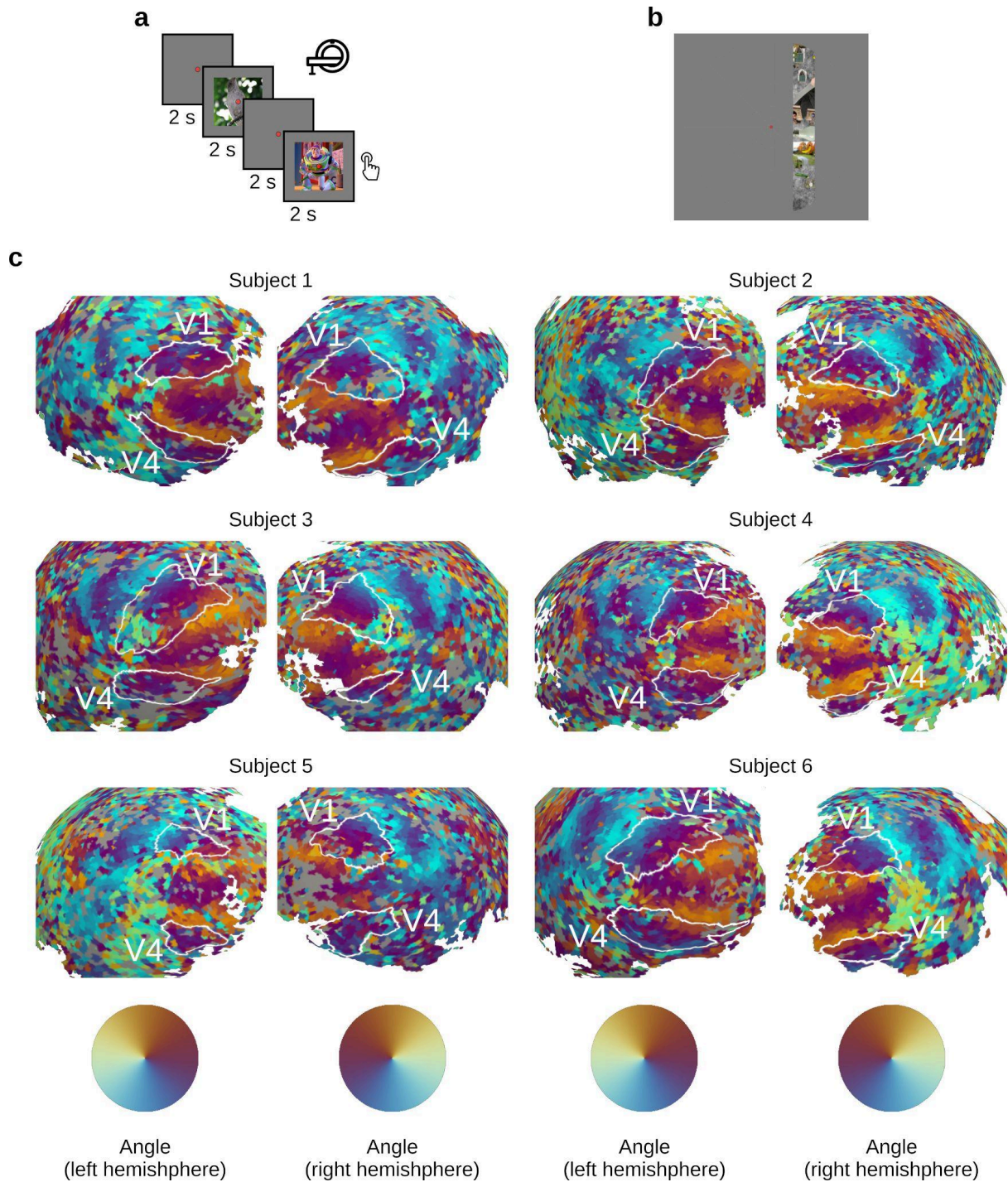
Supplementary Fig. 22 | Multivariate RNC controlling and baseline images for the V2 vs. V4 comparison. **a**, Controlling and baseline images from multivariate RNC applied on the in silico fMRI responses for the 73,000 NSD images. **b**, Controlling and baseline images from multivariate RNC applied on the in silico fMRI responses for the 50,000 ImageNet validation images. **c**, Controlling and baseline images from multivariate RNC applied on the in silico fMRI responses for the 26,107 THINGS images.



Supplementary Fig. 23 | Multivariate RNC controlling and baseline images for the V3 vs. V4 comparison. **a**, Controlling and baseline images from multivariate RNC applied on the in silico fMRI responses for the 73,000 NSD images. **b**, Controlling and baseline images from multivariate RNC applied on the in silico fMRI responses for the 50,000 ImageNet validation images. **c**, Controlling and baseline images from multivariate RNC applied on the in silico fMRI responses for the 26,107 THINGS images.



Supplementary Fig. 24 | Relationship between multivariate RNC controlling images, fMRI responses and RSM entries. a, V1 and V4 subject-average RSMs for the multivariate RNC aligning images. **b**, Relationship between images with and without the sky on their upper half, and fMRI responses for voxels tuned to the higher and lower portion of the visual field. Due to retinotopy, uniform regions on a spatially constrained portion of the image led to suppressed responses for voxels tuned to the corresponding portion of the visual field. Thus, the response of voxels tuned to the upper portion of the visual field were consistently suppressed by images including the sky on their upper half, whereas the same images drove the response of voxels tuned to the lower portion of the visual field (since the lower portion of these images include objects). The opposite pattern was observed for images not including the sky. This led to highly positive correlations (and corresponding RSM entries) when correlating the voxel responses for two sky images, or for two no sky images, and to highly negative correlations when correlating the voxel responses for a sky image and a no sky image.



Supplementary Fig. 25 | fMRI experiments and polar angle maps. **a**, Experimental design. We presented the univariate and multivariate RNC controlling and baseline images during a target detection task, where we asked subjects to press a button whenever an image with Buzz Lightyear appeared on the screen. Each image was presented for two seconds, followed by two seconds of inter-stimulus interval. Subjects were asked to fixate a central red dot during the entire experiment. fMRI responses were collected during image presentation. **b**, Screenshot of the pRF experiment used to delineate areas V1 and V4. **c**, Polar angle maps and V1/V4 delineations. Results are shown on FreeSurfer's sphere surface.

	V1	V2	V3	V4
Subject 1	813 / 1,350 (60 %)	656 / 1,433 (46 %)	486 / 1,187 (41 %)	176 / 687 (26 %)
Subject 2	598 / 1,102 (54 %)	407 / 1,075 (38 %)	448 / 1,097 (41 %)	239 / 483 (49 %)
Subject 3	553 / 1,254 (44 %)	366 / 1,141 (32 %)	152 / 928 (16 %)	61 / 426 (14 %)
Subject 4	340 / 877 (39 %)	285 / 863 (33 %)	141 / 808 (17 %)	40 / 475 (8 %)
Subject 5	529 / 1,113 (48 %)	424 / 1,081 (39 %)	259 / 925 (28 %)	154 / 542 (28 %)
Subject 6	484 / 1,127 (43 %)	381 / 1,180 (32 %)	205 / 1,201 (17 %)	50 / 477 (10 %)
Subject 7	273 / 1,142 (24 %)	174 / 986 (18 %)	86 / 726 (12 %)	48 / 397 (12 %)
Subject 8	234 / 1,074 (22 %)	168 / 1,033 (16 %)	68 / 889 (7 %)	60 / 495 (12 %)

Supplementary Table 1 | In silico fMRI retained voxels. Each cell indicates the amount of retained voxels (i.e., voxels with noise ceiling signal-to-noise ratio (ncsnr) scores above 0.5) out of the total voxels, for a given subject and area.

	V1	V4
Subject 1	35 / 382 (9 %)	25 / 323 (8 %)
Subject 2	225 / 487 (46 %)	173 / 383 (45 %)
Subject 3	283 / 647 (44 %)	125 / 284 (44 %)
Subject 4	211 / 425 (50 %)	96 / 289 (33 %)
Subject 5	157 / 389 (40 %)	66 / 286 (23 %)
Subject 6	262 / 428 (61 %)	167 / 375 (45 %)

Supplementary Table 2 | In vivo fMRI retained voxels for the univariate RNC experiment. Each cell indicates the amount of retained voxels (i.e., voxels with noise ceiling signal-to-noise ratio (ncsnr) scores above 0.4) out of the total voxels, for a given subject and area.

	V1	V4
Subject 1	86 / 382 (23 %)	55 / 323 (17 %)
Subject 2	190 / 487 (39 %)	101 / 383 (26 %)
Subject 3	242 / 647 (37 %)	67 / 284 (24 %)
Subject 4	109 / 425 (26 %)	24 / 289 (8 %)
Subject 5	105 / 389 (27 %)	30 / 286 (10 %)
Subject 6	270 / 428 (63 %)	130 / 375 (35 %)

Supplementary Table 3 | In vivo fMRI retained voxels for the multivariate RNC experiment. Each cell indicates the amount of retained voxels (i.e., voxels with noise ceiling signal-to-noise ratio (ncsnr) scores above 0.4) out of the total voxels, for a given subject and area.